

Article

Temporal and Spatial Development of the EM Field in a Shielding Enclosure with Aperture after Transient Interference Caused by a Subnanosecond High-Energy EM Plane Wave Pulse

Magdalena Budnarowska *  and Jerzy Mizeraczyk 

Department of Marine Electronics, Gdynia Maritime University, Morska 83, 81-225 Gdynia, Poland;
j.mizeraczyk@we.umg.edu.pl

* Correspondence: m.budnarowska@we.umg.edu.pl



Citation: Budnarowska, M.; Mizeraczyk, J. Temporal and Spatial Development of the EM Field in a Shielding Enclosure with Aperture after Transient Interference Caused by a Subnanosecond High-Energy EM Plane Wave Pulse. *Energies* **2021**, *14*, 3884. <https://doi.org/10.3390/en14133884>

Academic Editor: Andrea Mariscotti

Received: 3 May 2021

Accepted: 25 June 2021

Published: 28 June 2021

Publisher's Note: MDPI stays neutral with regard to jurisdictional claims in published maps and institutional affiliations.



Copyright: © 2021 by the authors. Licensee MDPI, Basel, Switzerland. This article is an open access article distributed under the terms and conditions of the Creative Commons Attribution (CC BY) license (<https://creativecommons.org/licenses/by/4.0/>).

Abstract: A proper assessment of the shielding effectiveness of an enclosure with aperture under subnanosecond transient interference requires a better understanding of the coupling and development mechanisms of the EM field induced inside the enclosure. In this paper, the results of a numerical study of the temporal and spatial development of the electromagnetic (EM) field in a shielding enclosure with aperture after transient interference caused by a subnanosecond high-energy EM plane wave pulse are presented. The interference pulse had Gaussian distribution of the electric and magnetic fields with amplitudes of 10^6 V/m and $2.68 \cdot 10^3$ A/m, respectively. The maximum pulse power density was 2.68 GW/m². The novelty of this study was 2D and 3D images, which visualized the temporal and spatial build-up of electric and magnetic fields in the shielding enclosure within 90 ns after the transient interference. This is 58 times longer than the time needed by any EM wave to travel the distance between the front and rear walls of the enclosure. The presented images, showing the EM field morphology over a relatively long period of time, were crucial for understanding the EM field build-up process inside the shielding enclosure with aperture. They revealed the existence of two unknown phases of the EM field build-up in the enclosure with aperture. We call these two phases the wave phase and the interference phase. In the wave phase, the EM field is generated in the form of so-called primary and secondary wave pulses, traveling towards the enclosure rear wall. In the interference phase, the EM field has the form of temporally and spatially varying pulse-like interference (size-limited) patterns of the associated electric and magnetic fields. The EM field induced in the enclosure is long-lasting compared to the interference pulse duration. The amplitudes of the electric and magnetic fields decreased about threefold in 5 ns and 30-fold in 90 ns, thus exhibiting a severe EM hazard for much longer than the external interference duration. For a long period of time, the highest EM field amplitudes would change their locations in the enclosure, which makes it difficult to assess the shielding effectiveness on the basis of classical definitions. The existence of the long-lasting temporally and spatially varying EM field induced in the enclosure with aperture by the subnanosecond transient interference, visualized in detail in this paper, confirms that a new definition and measurement methods of shielding effectiveness under transient conditions are needed. The obtained results provide a source of data that can be useful when working on the introduction of time-domain parameters to evaluate the transient shielding effectiveness in the case of the ultrashort EM interference.

Keywords: electromagnetic interference; EMI; high-power electromagnetic pulse; shielding enclosure with aperture; shielding box; electromagnetic field shielding; numerical simulation of EM field; CST Studio

1. Introduction

The operation of technologically advanced electronic infrastructure is exposed to threats from various natural and intentional electromagnetic (EM) environments, which may cause malfunction or damage [1,2].

The sources of natural EM environments are all kinds of atmospheric electric discharges (lightning, solar flares, and auroras). It is reasonable to include anthropogenic EM interferences generated by manmade devices into the natural EM environments. Examples of sources of EM interferences resulting from human activity are ignition systems in internal combustion engines; telecommunication networks, including mobile phone communication, radio, and television transmitters; and electric networks [3,4].

The intentional EM interferences are generated by EM environments created with the intent to disrupt or destroy electronic infrastructure. In accordance with their intended use, they are characterized by significantly higher EM radiation than natural EM environments. The EM radiation generated by such environments is called high-power EM radiation [2].

The high-power intentional EM environments are generated by means of nuclear or non-nuclear EM pulses. The intentional non-nuclear EM pulses are generated by various types of electric and magnetic methods [4].

It is known that the extent of damage caused to advanced electronic devices depends not only on the power (or energy) of EM radiation pulses but also on their time and frequency characteristics. The vast majority of advanced electronic devices are sensitive to EM interference in selected frequency ranges from several tens of MHz to 10 GHz. Therefore, the degree of threat to electronic infrastructure from high-power EM pulses also depends on their frequency spectrum and its matching to the frequency susceptibility spectrum of the electronic object in which it is the most vulnerable to EM threats.

When analyzing EM environments according to the frequency ranges they cover, they can be divided into narrowband and broadband.

The unintentional narrowband EM environment, called a high-intensity radiated field, is generated by radar systems, radio and television transmitters, etc. The intentional narrowband environments are produced by sources that generate sub- and microsecond sine-wave pulses of high-power microwave frequencies called high-power microwave pulses.

Depending on the width of the frequency spectrum range, the broadband EM environments are divided into environments with a moderate, ultra-wide, and hyper-wide frequency spectrum. The broadband environments include those created by natural atmospheric discharges (i.e., lightning), intentional nuclear explosions outside the earth's atmosphere, and intentional non-nuclear sub- and nanosecond ultra-wideband (UWB) short pulses [2].

The most likely intentional high-power EM interference will have the form of a single pulse or a sequence of sub- and nanosecond UWB pulses forming a broadband frequency spectrum ranging from 0.2 to several GHz, sub- and microsecond sinusoidal pulses of a narrow frequency band (about 1% of the sinusoidal frequency) in the range of 0.3–15 GHz, and several hundred nanosecond pulses of attenuated sinusoids forming a moderate spectral band environment up to several hundred MHz in the range from 100 MHz to 1 GHz. Producing the EM interference in the form of sub- and nanosecond UWB pulses requires the use of high-tech sources of such pulses. It is different with the availability of the sources of sub- and microsecond sinusoidal pulses and several hundred nanosecond damped sinusoidal pulses, the manufacturing of which does not require such advanced technology. Publicly available literature reports a number of cases of EM attacks, using relatively easily available high-power EM pulse sources [5,6]. These attacks targeted the electronic infrastructure securing gaming machines, jewelry shops, banking systems, police telecommunications systems, anti-theft systems in luxury cars, etc. This shows that, nowadays, the real threat to electronic infrastructure from intentional high-power EM environment attacks no longer concerns only electronic military structure but also a variety of sectors, including consumer and industrial electronics and emergency services.

The widespread threat of EM attacks calls for intensified development of appropriate countermeasures.

There is a plausible opinion that the greatest ‘havoc’ in the operation of electronic objects is caused by short-duration pulses with high power density, i.e., high electric field strength [6]. High and rapidly changing electric field strength of EM pulses induces high potentials in electronic components and systems, which initiate overvoltage waves, electric breakdowns in semiconductor junctions, and electrostatic discharge, resulting in the operational disruption of an electronic system in the mildest case, and eventually its damage. Therefore, it is the maximum value of the electric field strength of the EM pulse, not its energy, that is considered to be one of the most important parameters in assessing the degree of EM hazard for electronic objects.

High effectiveness in the protection of electronic objects against high-power EM pulses is provided by different types of metal enclosures, such as shielding enclosures or boxes inside which sensitive electronic objects can be placed. The walls of a shielding enclosure are made of highly conductive metal to absorb the EM energy of the incoming high-power EM pulses and cause an electric current on the surface of the enclosure body [5,7–9]. This current is absorbed by an earth connection or a virtual ground plane, whereby the incoming high-power EM pulses do not reach the sensitive stored inside the enclosure. Similarly, the sensitive EM signals formed inside the enclosure are effectively protected from being transmitted uncontrolled outside the box (signal transmission takes place through shielded wire connections).

Larger EM shielding enclosures are typically used to protect complex electronic systems in government organizations, police, military and intelligence agencies, banking systems, etc. Recently, those in charge of consumer and industrial electronics and emergency services have become increasingly interested in EM shielding for small devices, such as laptops, tablets, smartphones, ID cards, car keys, etc. [10,11].

The fully enclosed perfectly conductive shielding boxes provide an ideal protection for all but low-frequency magnetic fields. However, such fully enclosed shielding boxes are not practical. They need to have several functional structures such as apertures (e.g., for ventilation) and wire connections for inside–outside communication. For this reason, the EM protection cannot be perfect and the level of EM interference from the outside depends on the coupling of the outside EM interference into the enclosure and the susceptibility of the protected devices placed inside to the temporal, spatial, and frequency characteristics of the outside EM interference. Usually, the susceptibility of the enclosure with apertures or penetrations to the outside interference is determined by the so-called shielding effectiveness (SE) of the enclosure.

The temporal, spatial, and frequency characteristics of the incoming interference is crucial for its coupling into the enclosure with an aperture. As mentioned above, the most likely intentional high-power EM interference will be in the form of sub- and nanosecond pulses of UWB EM fields in the frequency range 0.2 to a few GHz, sub- and microsecond pulses of sinusoids of a narrow frequency band (about 1% of the sinusoidal frequency) in the range of 0.3–15 GHz, and several hundred nanosecond pulses of attenuated sinusoids forming a moderate spectral band environment up to several hundred MHz in the range from 100 MHz to 1 GHz. Therefore, the susceptibility of the shielding enclosure with aperture to each of these types of pulses, having different temporal, spatial, and frequency characteristics, is expected to be different. To assess properly the shielding effectiveness of an enclosure with aperture under transient interference, one requires a better understanding of the coupling and development mechanisms of the EM field induced inside the enclosure. This refers, in particular, to the case when the external interference is caused by ultrashort EM field pulses, for which duration is much shorter than the time required for the pulse to pass fully through the enclosure. An example of such pulses is sub- and nanosecond pulses of UWB EM fields, listed above as the most likely intentional high-power EM interference. In contrast to the cases of EM interference by relatively long pulses (e.g., [12]), there is the lack of research on the interaction of the extra-short pulses with shielding enclosures with apertures.

In this paper, we study the interaction of an ultrashort transient interference caused by a subnanosecond transient EM plane wave pulse of a Gaussian distribution of electric and magnetic fields, with a small rectangular enclosure ($455 \times 50 \times 463$ mm) having a rectangular aperture. The maximum power density of the subnanosecond EM plane wave pulse is 2.68 GW/m^2 . Such an EM wave pulse is a typical intentional UWB high-power EM pulse, which is one of the most likely intentional EM interferences. The aim of the study was to visualize the temporal and spatial development of the electromagnetic (EM) field in the shielding enclosure with aperture after a transient interference caused by the subnanosecond high-energy EM plane wave pulse. It was expected that the results obtained will be essential for a better understanding of the EM field build-up process inside the shielding enclosure with aperture, which will aid in the evaluation of the shielding effectiveness under ultrashort transient interference conditions. The study was carried out using the numerical simulation method offered by CST Studio software.

It was expected that the results obtained will be essential for a better understanding of the EM field build-up process inside the shielding enclosure with aperture, which will aid in the evaluation of the shielding effectiveness under ultrashort transient interference conditions.

2. Shielding Enclosure with Aperture

The geometry of the shielding enclosure with aperture (hereinafter called the enclosure for brevity) is shown in Figure 1, in which the enclosure is placed in the rectangular coordinate system in such a way that the center of the enclosure coincides with the center point A (0,0,0) of the coordinate system. The external dimensions of the enclosure are width = 455 mm (x (−227.5 mm, +227.5 mm)), height = 50 mm (y (−25 mm, +25 mm)), depth = 463 mm (z (−231.5 mm, +231.5 mm)). They were selected so that the enclosure could fit a standard 17-inch laptop, a mobile phone, and two portable computer memory drives. In the center of the front wall of the enclosure, there is a rectangular 30×80 mm aperture that simulates a ventilation and wire connection, operating in the real shielding enclosures. The area of the rectangular aperture is approximately 10% of that of the enclosure front wall. The thickness of the shielding enclosure walls is 1 mm. The enclosure walls are made of a material with infinite conductivity, called the perfect electric conductor (PEC). This means that the absorption loss of the EM field on the enclosure walls is zero.

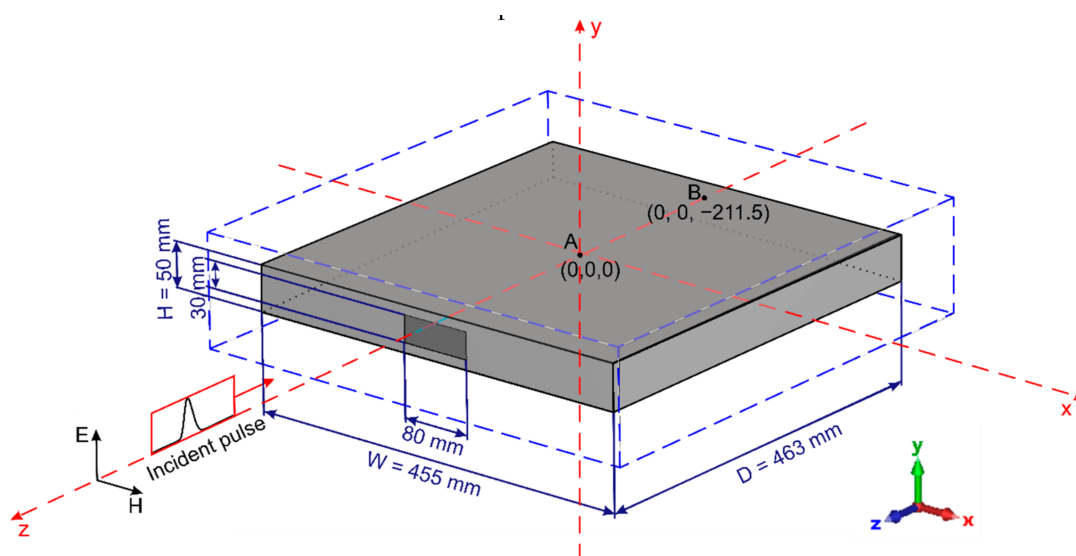


Figure 1. The geometry of the enclosure with aperture in the rectangular coordinate system. The computation area is marked in blue dashed lines. The electric field strength vector E is directed in the $+y$ direction. The magnetic strength vector H is directed in the $+x$ direction. Point A is the center of the enclosure. Point B marks the place where the substantial EM wave interference took place (see Section 5).

3. Simulation Procedure

The numerical simulation of the temporal and spatial development of the EM field in the enclosure after interference of the high-energy EM pulse was performed using CST Studio software equipped with the MW and RF and Optical module for modeling and comprehensive simulations of high-frequency EM fields of 3D objects [13].

The simulation involved performing numerical calculations using a time domain solver. When the simulations of high-frequency electromagnetic fields of 3D objects on the basis of calculations of the numerical solutions of Maxwell's equations are performed, it is well known that the quality and type of mesh used for discretizing the computational volume are very important. Meshing in the time domain provides a compromise between speed, accuracy, and memory requirements. In the numerical simulation, we used a hexahedral mesh type, which is discretized by means of variable size rectangular cuboids (a small volume in space where the electric and magnetic fields are computed). In order to optimize the mesh with regard to speed, accuracy, and memory requirements, we introduced 15 cells per wavelength, near and far from the object, and a minimum cell size by dividing the maximum cell size by 15. In our simulations, we used a singularity model for PEC and lossy metal edges. The final mesh has 20, 127, and 240 mesh cells.

The enclosure was placed symmetrically in a computational cell with the dimensions $\times (-235 \text{ mm}, +235 \text{ mm})$, $y (-32.5 \text{ mm}, +32.5 \text{ mm})$, $z (-239 \text{ mm}, +239 \text{ mm})$ (see Figure 1). The computation area ($470 \times 65 \times 478 \text{ mm}$) is marked with blue dashed lines in Figure 1. The front plane of the computation area is set to $z = +239 \text{ mm}$. The subnanosecond high-power EM interference plane wave pulse (called the incident pulse in the following sections on the simulations and their results) propagates perpendicularly towards the enclosure front wall (i.e., in the $-z$ direction). It is assumed that the electric field strength vector E of the incident pulse is directed in the $+y$ direction (correspondingly, the magnetic field strength vector H is directed in the $+x$ direction).

The numerical simulation was mainly focused on 2D and 3D visualization of the temporal and spatial development of the EM field induced by the incident pulse inside the enclosure.

4. Parameters of the Incident EM Plane Wave Pulse

The incident subnanosecond high-power EM plane wave pulse has a Gaussian distribution of the electric and magnetic fields' strengths. The maximum electric and magnetic field strength amplitudes of the incident pulse are described by the following equation:

$$\frac{A(t)}{A_{\max}} = e^{-\frac{4 \ln 2 (t-t_{\max})^2}{\tau^2}}, \quad (1)$$

where

$A(t)$ —the amplitude of the electric or magnetic field strength;

A_{\max} —the maximum amplitude of the electric field or magnetic field strength;

t_{\max} —the time when the amplitude of the electric or magnetic field strength reaches its maximum value;

τ —the full width at half maximum of the incident pulse.

The parameters of the incident pulse (Figure 2) were as follows: the maximum electric field strength amplitude— 10^6 V/m , the maximum magnetic field strength amplitude— $2.68 \cdot 10^3 \text{ A/m}$, the maximum pulse power density— 2.68 GW/m^2 , time when the amplitude of the electric or magnetic field strength reaches maximum value— $t_{\max} = 0.1779 \text{ ns}$, the full width at half maximum (FWHM) of the incident pulse— $\tau = 0.0804 \text{ ns}$, the pulse rise time— $\tau_r = 0.058 \text{ ns}$, the pulse fall time— $\tau_f = 0.058 \text{ ns}$.

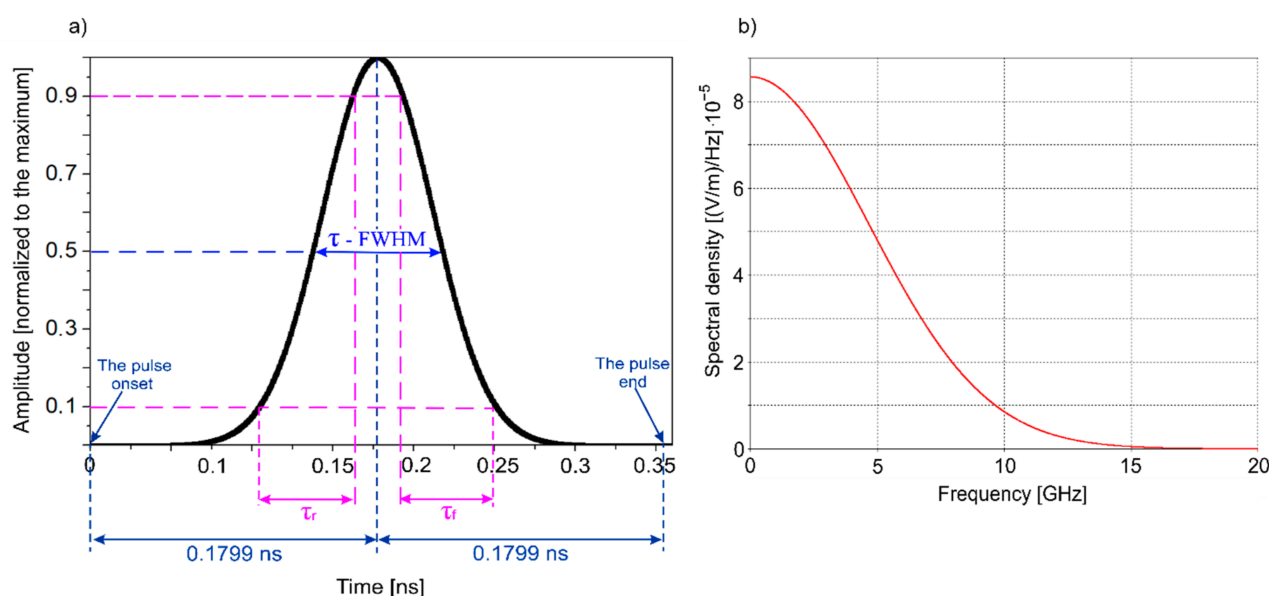


Figure 2. The normalized incident Gaussian EM plane wave pulse: (a) the time dependence of the electric field strength (or the magnetic field strength) and (b) the spectral density of the electric field strength of the incident Gaussian EM plane wave pulse.

For clarity, we defined the incident pulse onset (or starting point) as a point preceding the pulse maximum by 0.1779 ns (Figure 2). Similarly, the end of the incident pulse was defined as a point 0.1779 ns after the pulse maximum. The electric and magnetic field strengths were practically zero at both points. We set the time to $t = 0$ when the onset of the incident pulse reached the front plane of the enclosure, in other words, when the pulse maximum was 0.1779 ns in front of the enclosure front plane.

The spectrum density of the incident Gaussian EM plane wave pulse is shown in Figure 2. It shows that the spectrum density of the electric field strength of the incident Gaussian EM plane wave pulse ranged from zero to about 15 GHz, covering the susceptibility spectra of most electronic devices.

5. Results

The obtained numerical results show that the incident pulse was initiated in the enclosure with aperture a series of associated electric E and magnetic H fields, which formed EM wave pulses propagating from the aperture towards the rear wall of the enclosure. We call these waves the primary waves. The primary waves were easily visible in the recorded images as long as their wings did not reflect off the sidewalls of the enclosure. The resulting reflected waves, called secondary waves, travelled obliquely in the enclosure, causing wave interferences (the constructive or negative superposition of waves) with subsequent primary waves. The resulting interference patterns in the recording images disrupted the observation of not only the primary but also the secondary waves. The observation of both types of waves became more difficult after the reflection of the primary waves (and then the secondary waves) from the rear wall and their return towards the front wall. Then, the number of interfering waves traveling in different directions increased significantly, resulting in an increasing number of interference patterns. After subsequent reflections from the enclosure walls, the recorded images showed the interference patterns rather than the traveling waves. Therefore, after the first phase, called the wave phase of the development of the EM field in the enclosure, which can be described in terms of primary and secondary EM waves, the following development phase (called the interference phase) should be considered in terms of temporally and spatially varying patterns of the associated electric and magnetic fields.

The simulation results presenting the formation, development, and decay of the EM in the enclosure were recorded as video films: (A) 3D electric field amplitude, (B) 3D magnetic field amplitude, (C) 2D electric field amplitude, and (D) 2D magnetic field amplitude (Supplementary Materials). Scan the QR code below to watch the films (Scheme 1).



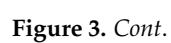
Scheme 1. QR code with link to video films.

It is worth watching these films to learn about the dynamics of the development of the electric and magnetic fields in the enclosure with aperture under the conditions of irradiation with a short-term EM pulse. A selection of representative frames from these movies is shown below.

The images in Figure 3 show separately the three-dimensional (3D) temporal and spatial development of the electric and magnetic fields in the enclosure with aperture for selected times after $t = 0$ (set when the incident plane wave pulse onset reaches the front plane of the enclosure). The position of the incident plane wave pulse versus time is marked on the upper wall of the enclosure. The images in Figure 3 show the amplitudes of the electric (left column) and magnetic (right column) fields. Other details about the electric and magnetic field structures developed in the enclosure can be easily found from the two-dimensional (2D) images or vector maps for selected cross sections of the enclosure interior shown in Figures 3–11.

Figure 3Ea (also Figure 4Ea) illustrates the initiation of the electric field in the vicinity of the aperture at a time of $t = 0.1375$ ns, i.e., at the moment when the half-maximum of the front part of the incident pulse passes the front wall plane of the enclosure. It is also instructive to observe this situation on the vector map of the electric field distribution in the $x = 0$ plane (Figure 5a), which, among other things, shows the polarization of the electric field in the created electric field structure. As seen in Figures 3Ea, 4Ea and 5a, the electric field at $t = 0.1375$ ns took the form of a flat dipole-like structure created between the electric charges gathered on the lower and upper edges of the aperture. The electric field direction in the dipole-like flat structure was the same as that of the incident pulse. The lower and upper edges of the aperture seemed to behave as a linear source of electric dipoles (Figure 6, $t = 0.1779$ ns).

As the incident pulse moved along the enclosure, the dipole-like flat electric field structure penetrated deeper inside the box. At $t = 0.1779$ ns, when the incident pulse maximum passed the enclosure front wall plane, the amplitude of the electric field in the enclosure front wall plane reached its maximum value, equal to the electric field amplitude of the incident pulse (Figures 3Eb, 4Eb and 5b).



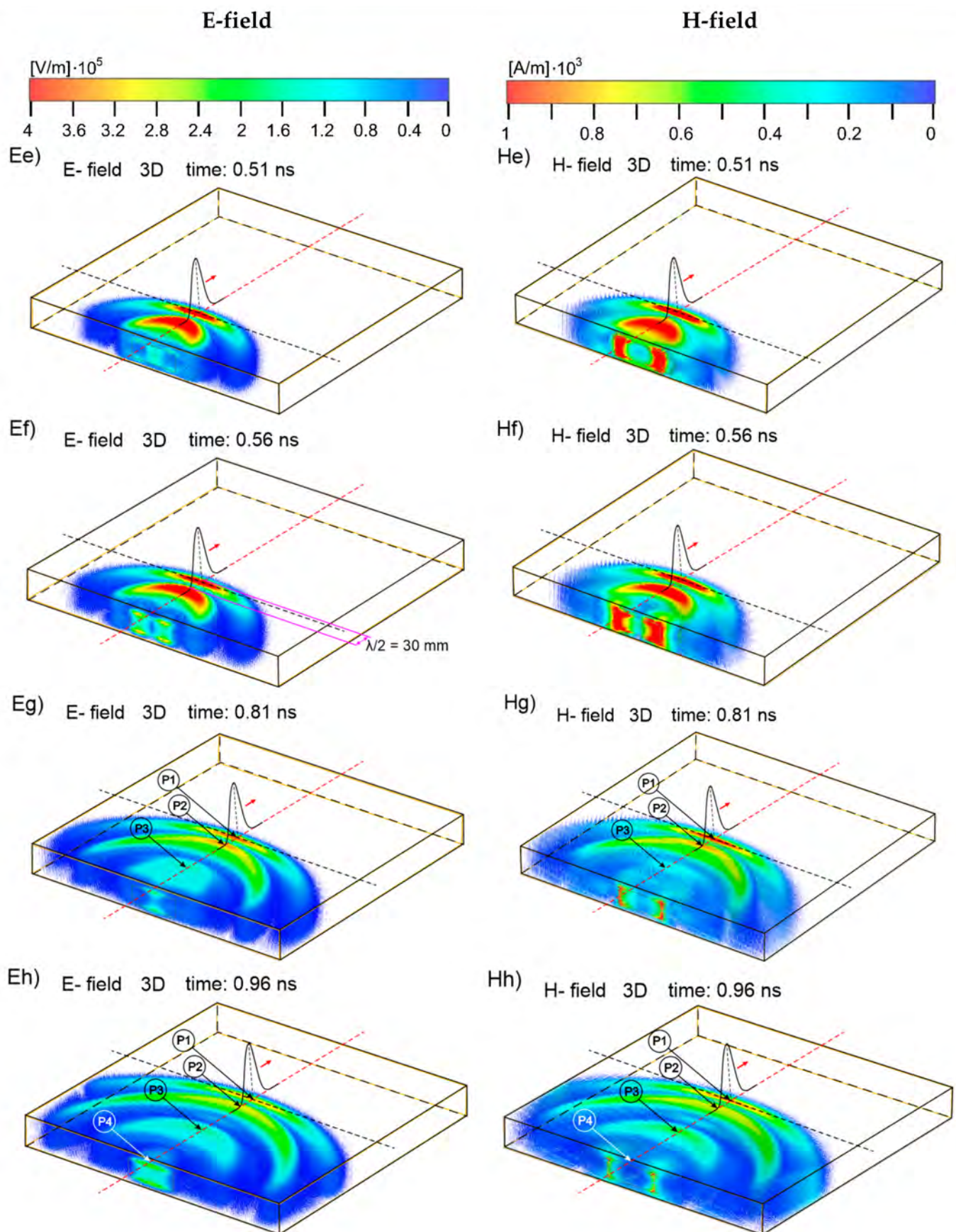


Figure 3. Cont.

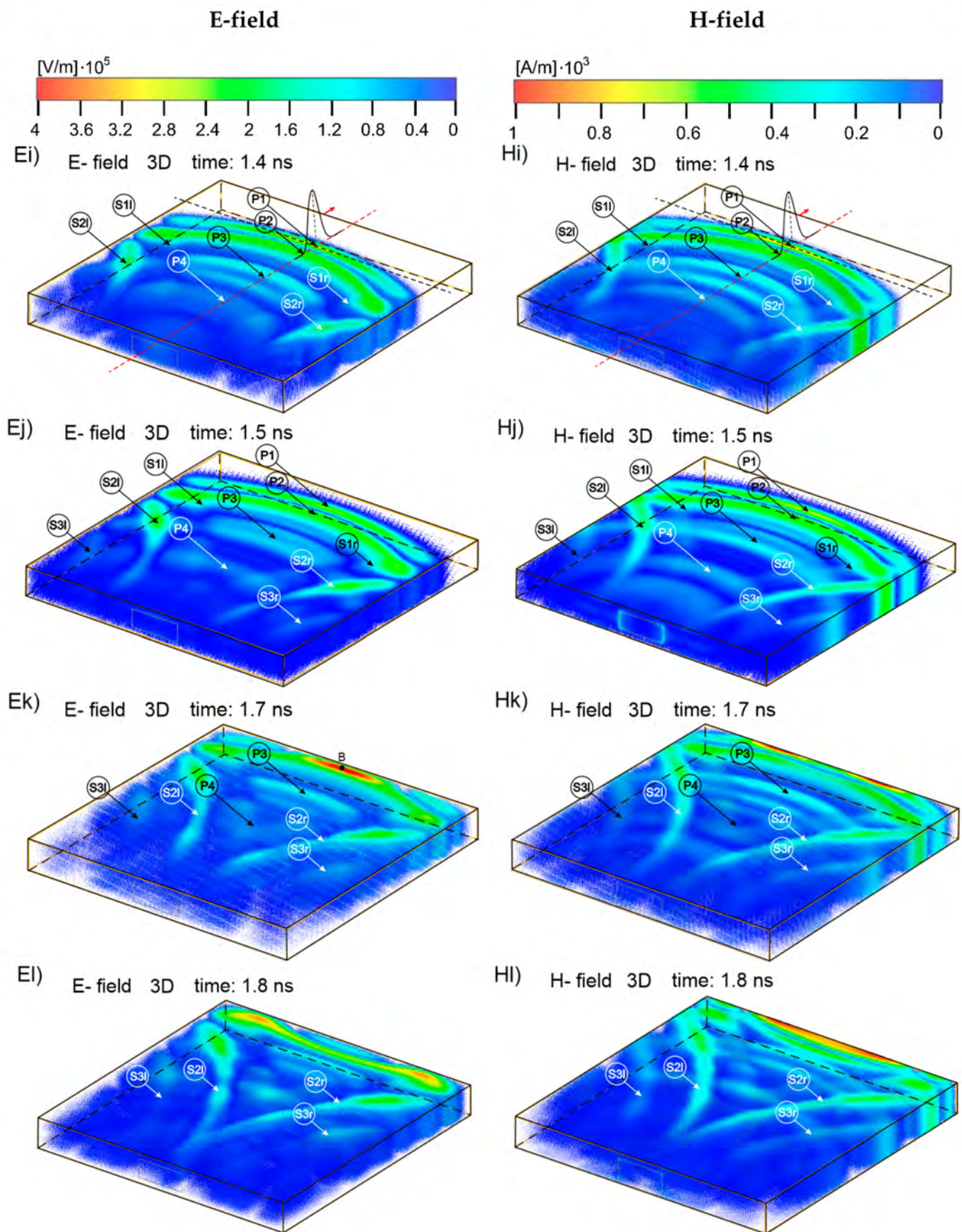
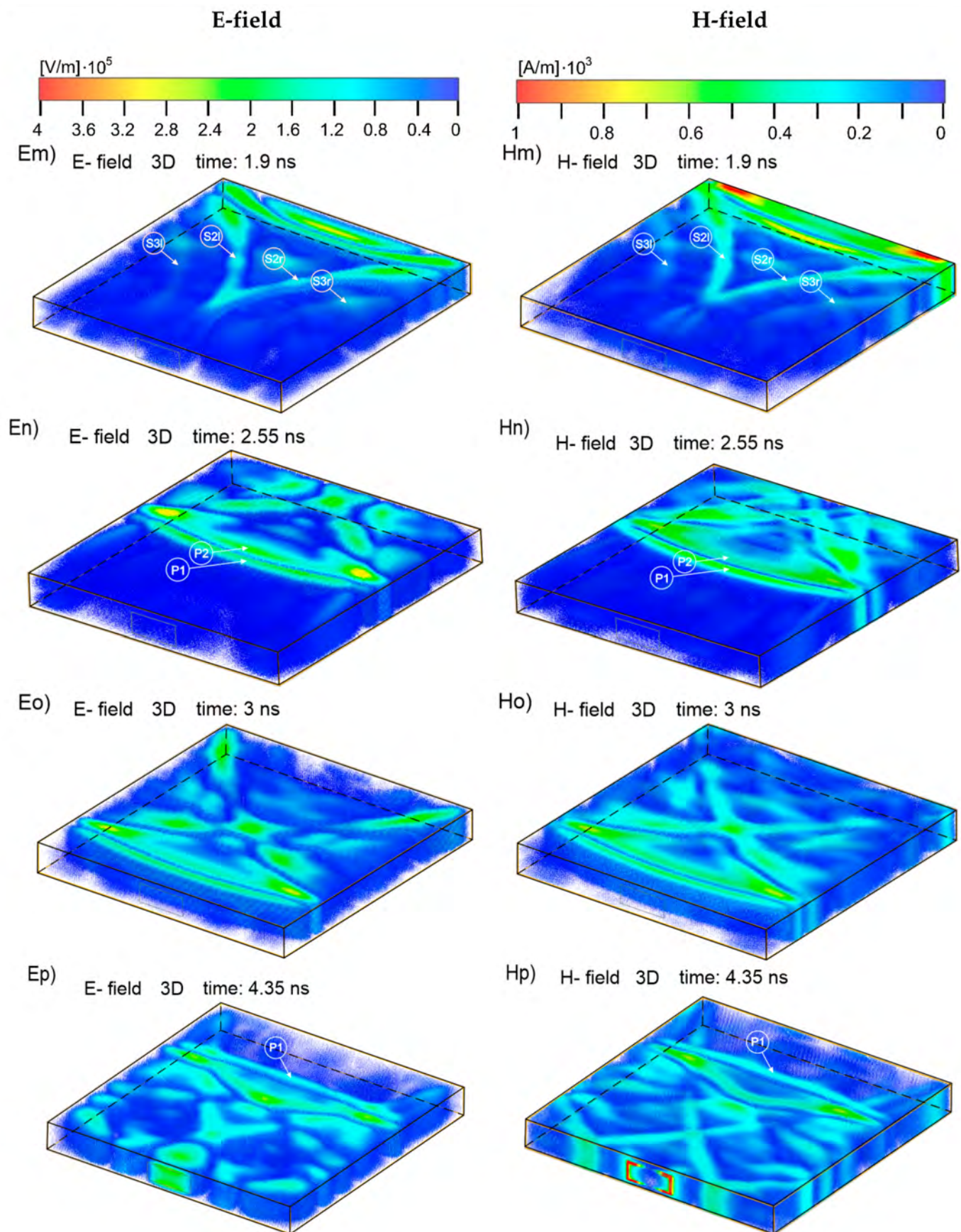


Figure 3. Cont.



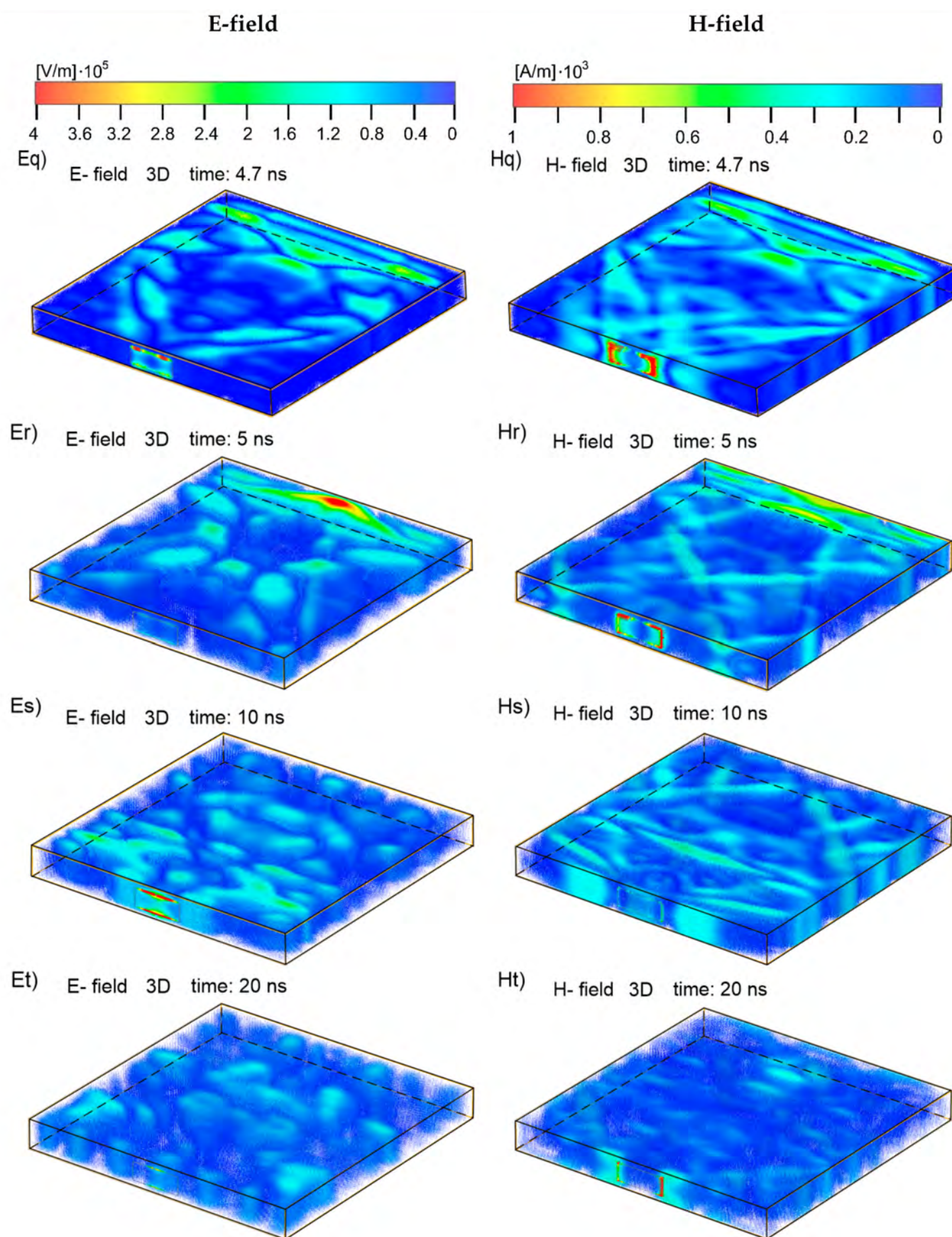


Figure 3. Cont.

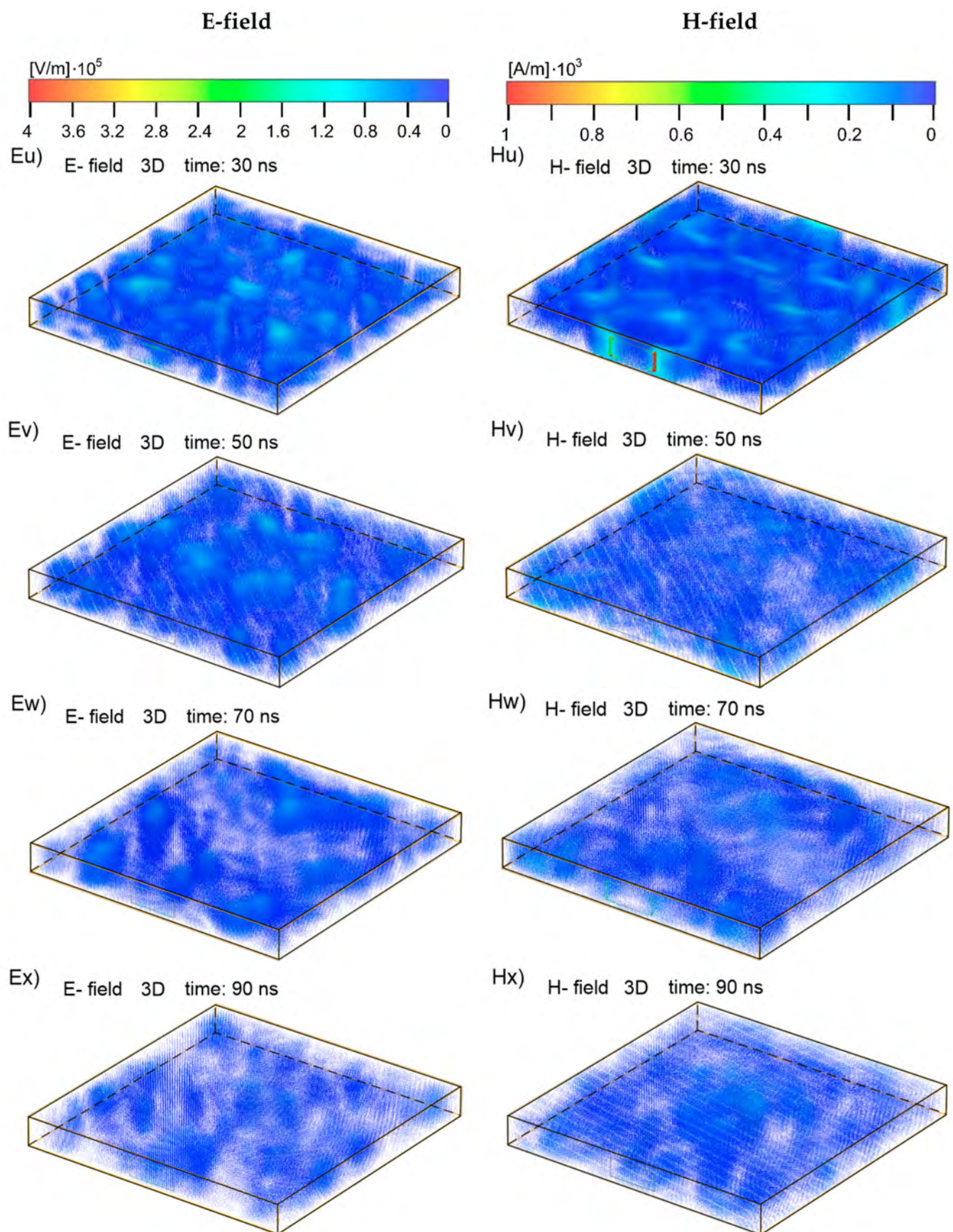


Figure 3. 3D development of the electric and magnetic fields in the enclosure. (Left column)—the electric field amplitude; (Right column)—the magnetic field amplitude. The current position of the incident pulse is shown.

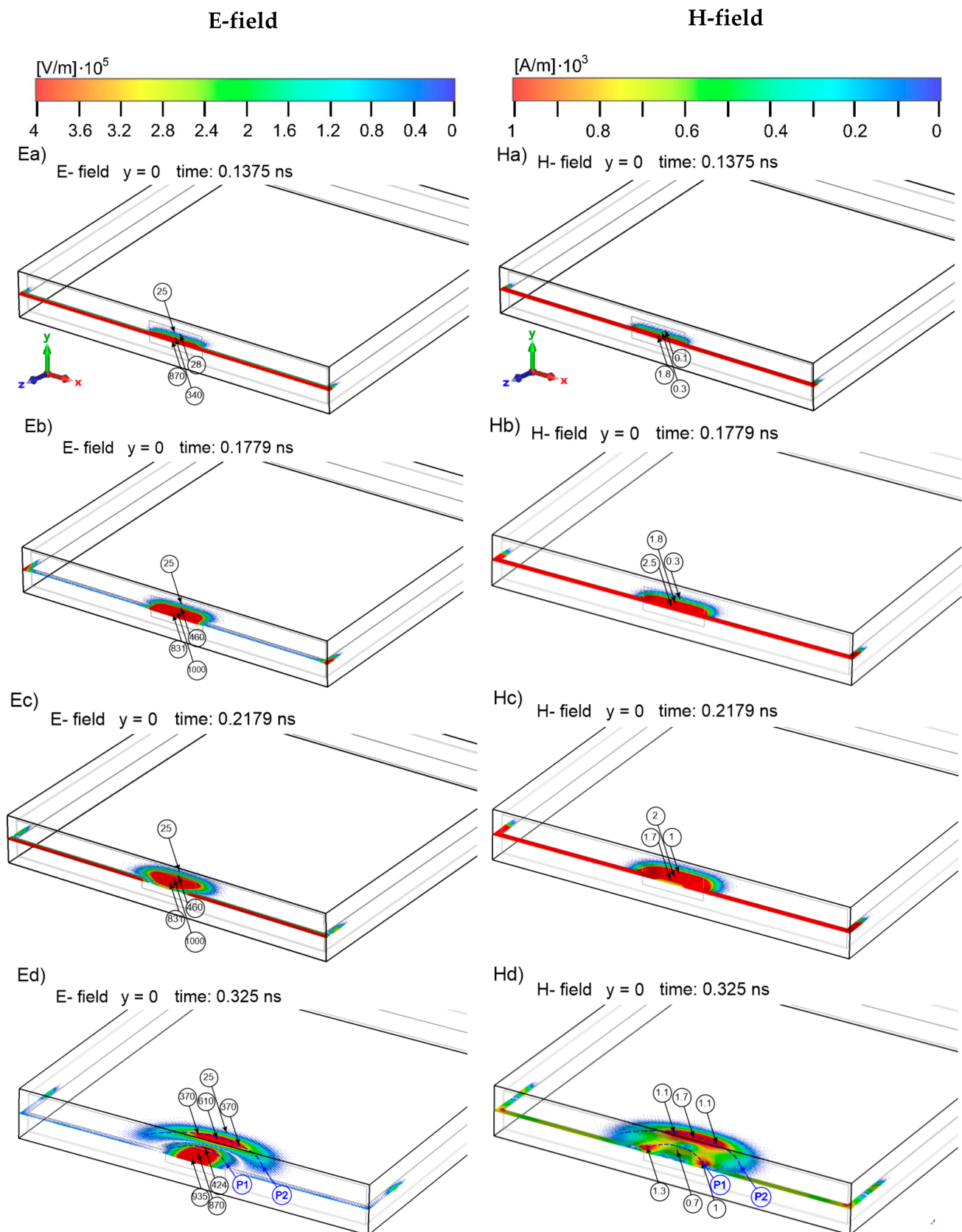


Figure 4. Cont.

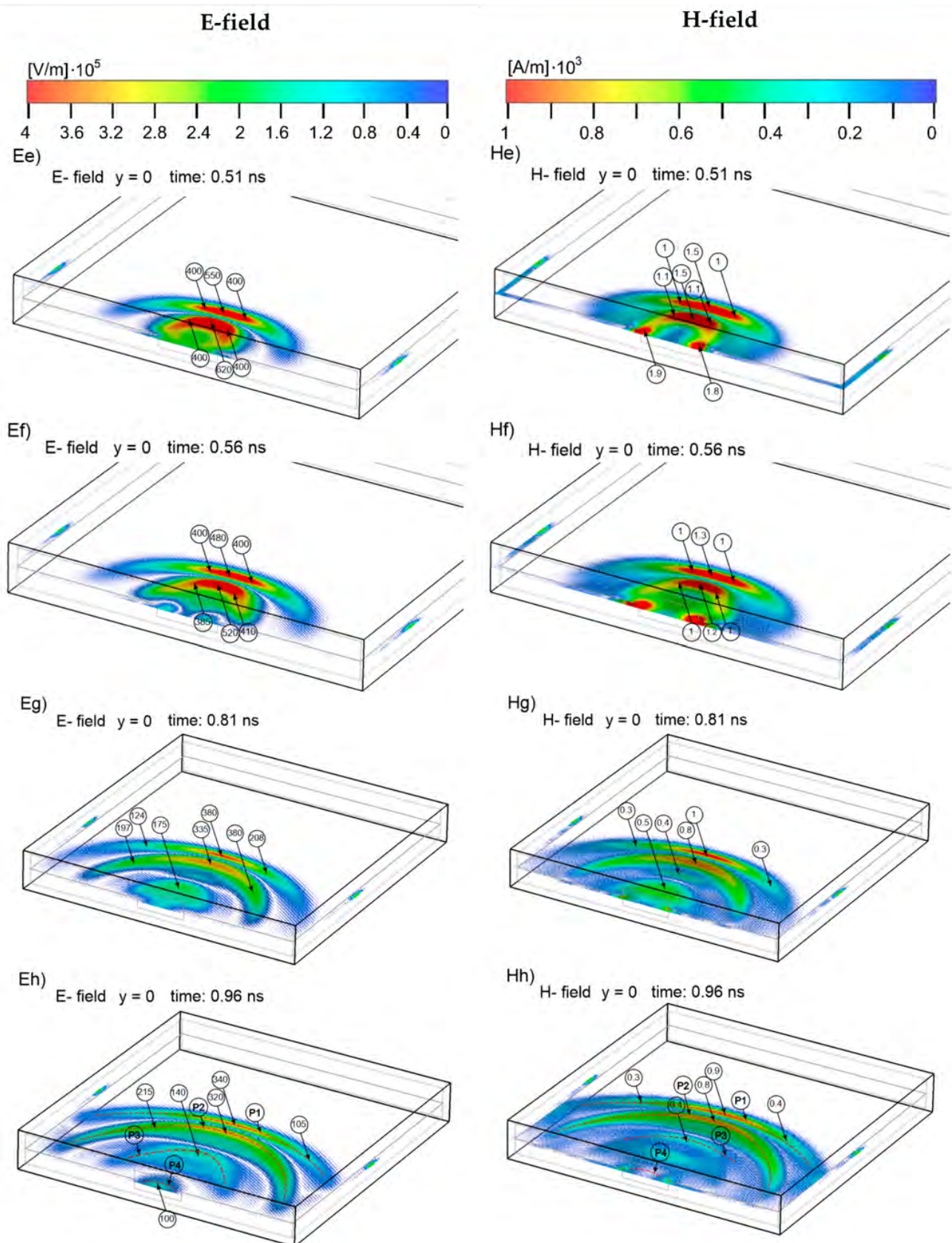


Figure 4. Cont.

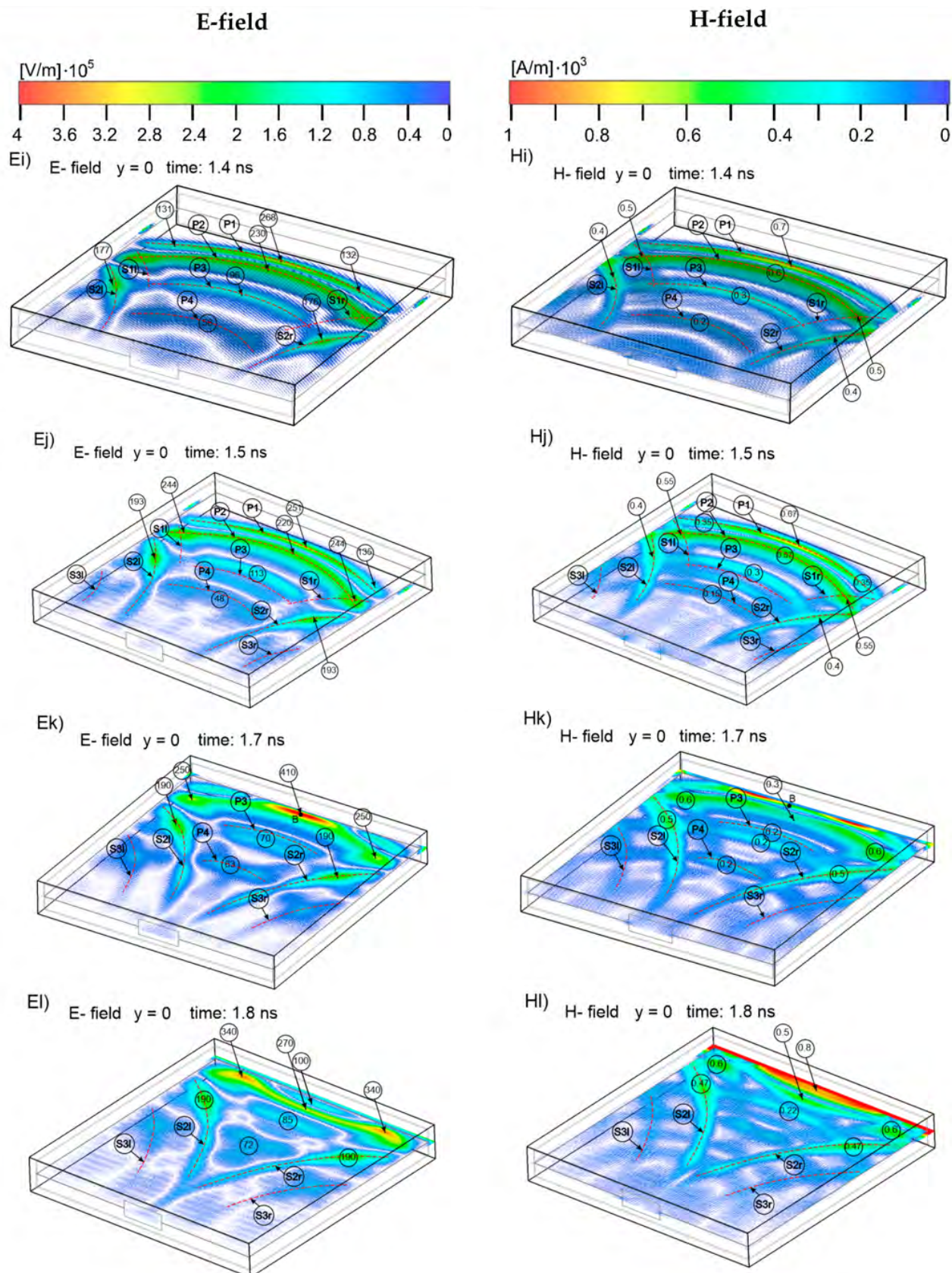


Figure 4. Cont.

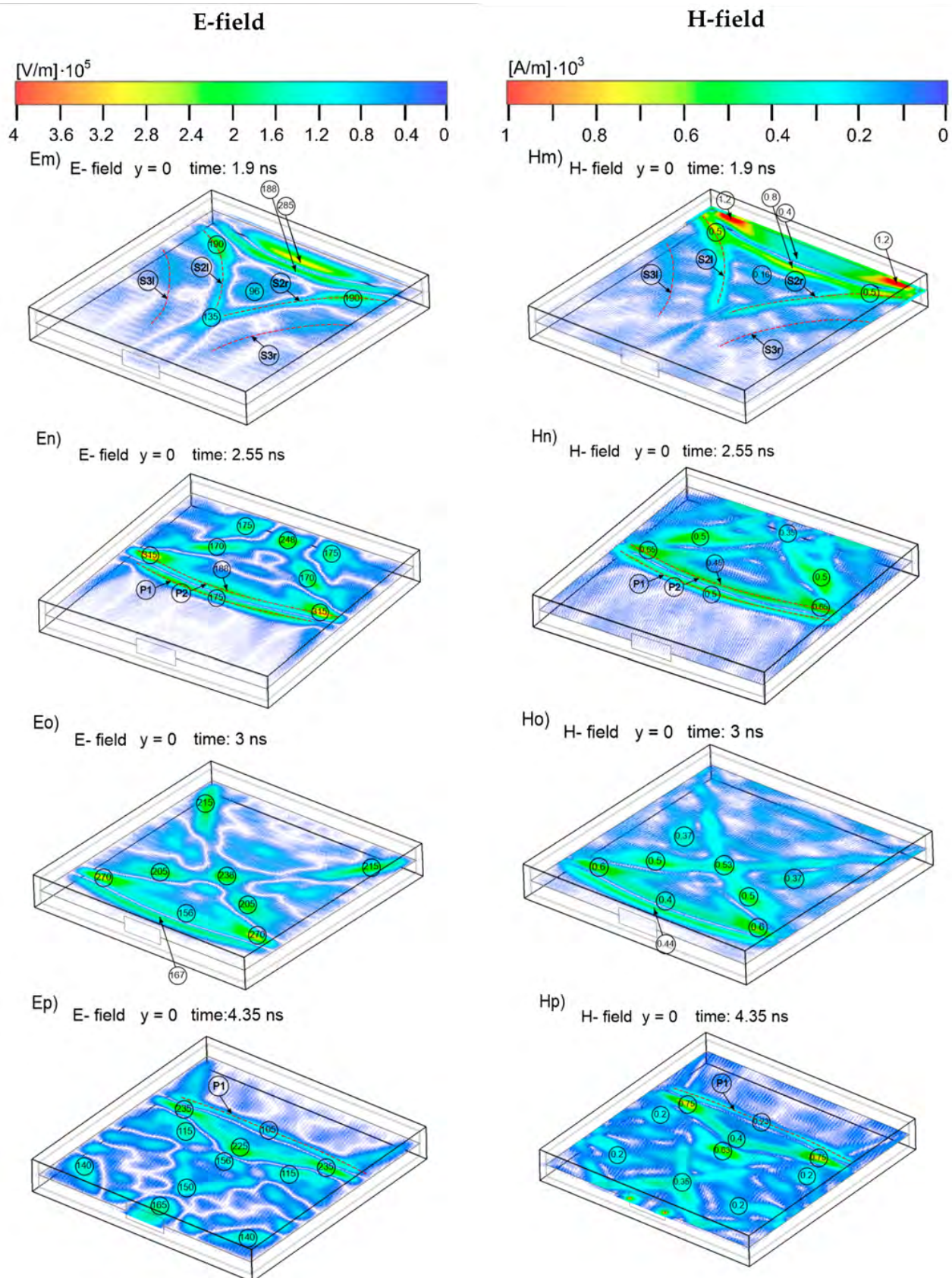


Figure 4. Cont.

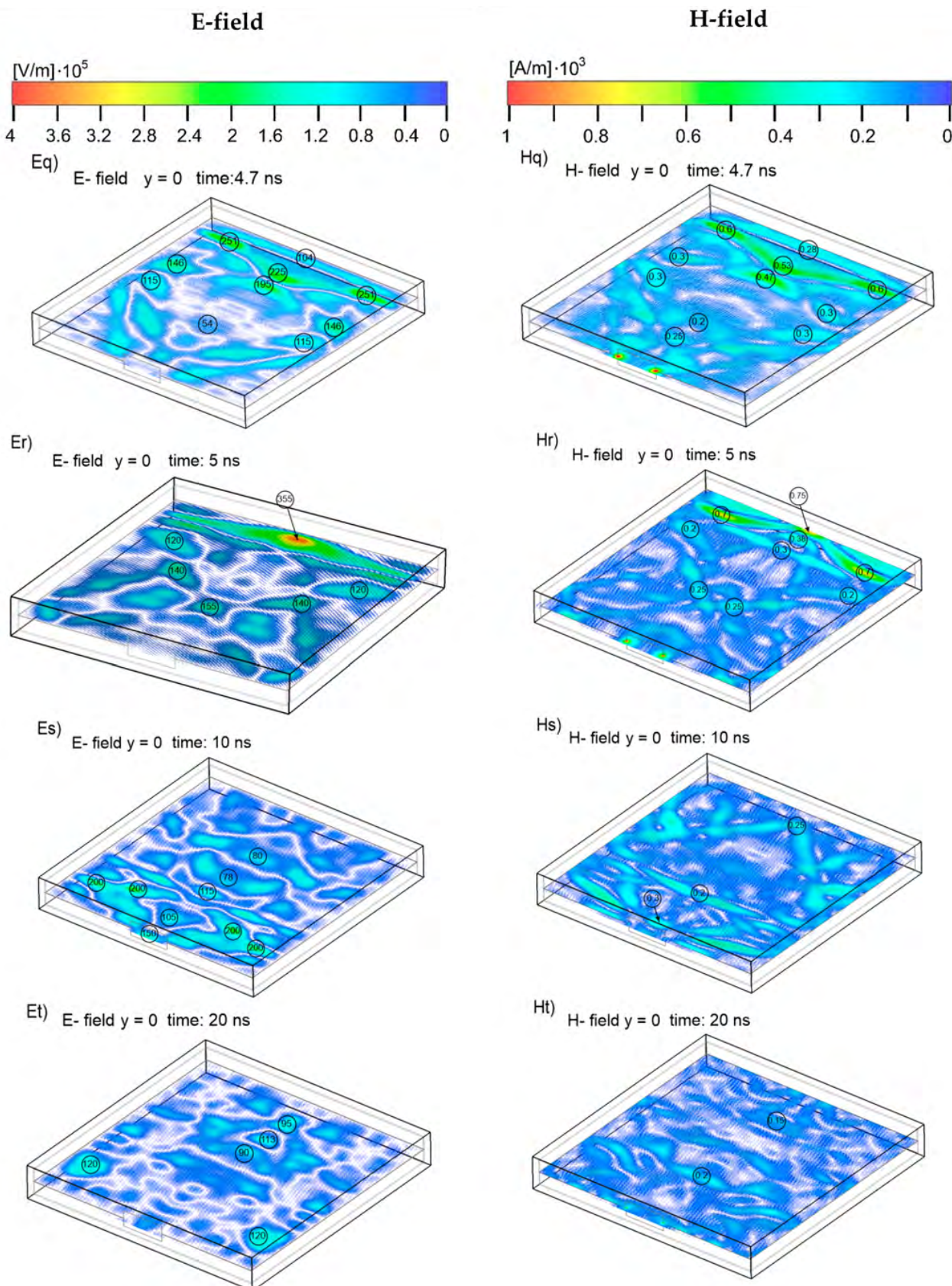


Figure 4. Cont.

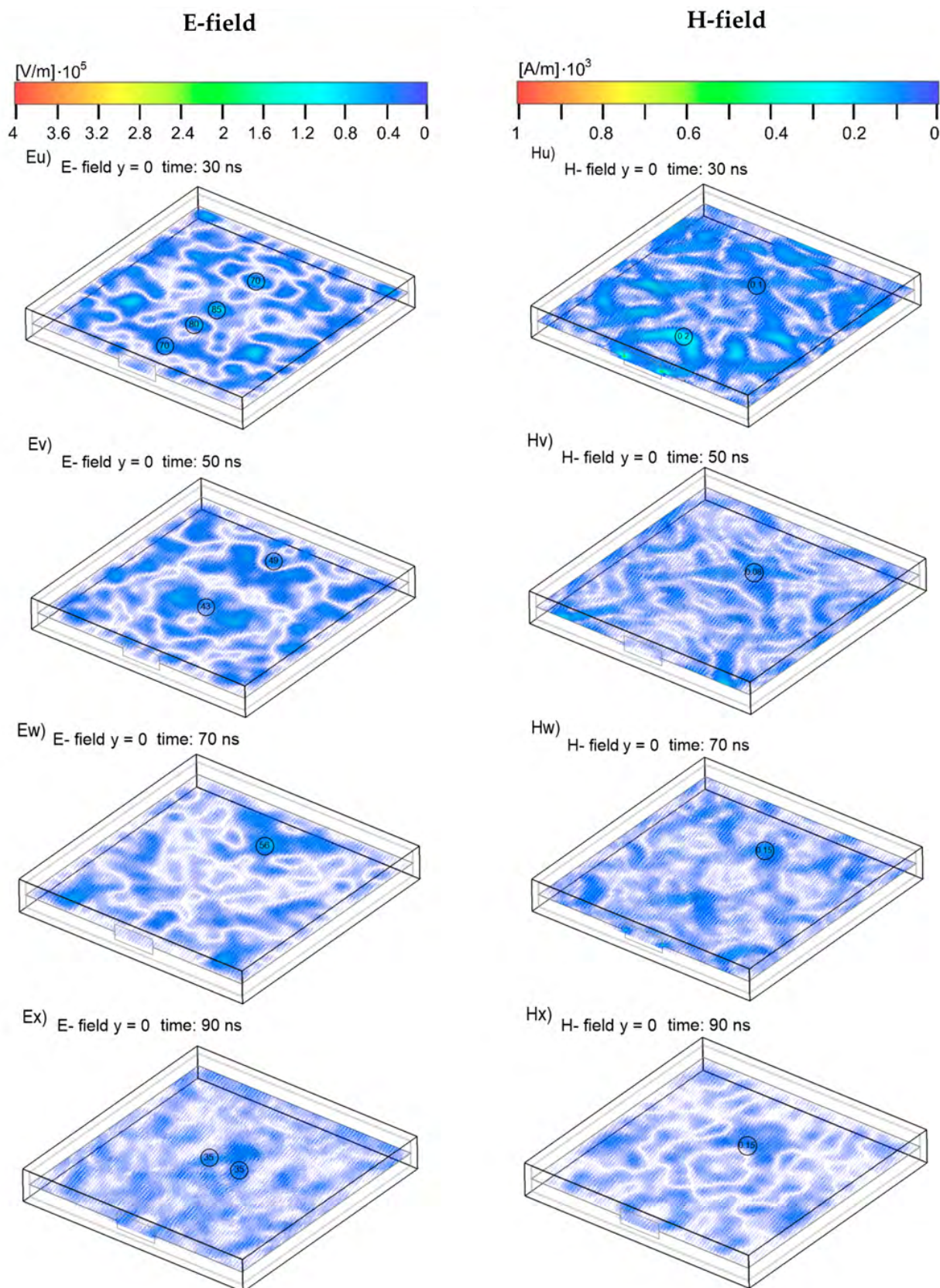


Figure 4. 2D development of the electric and magnetic fields in the enclosure. (**Left column**)—the electric field amplitude; (**Right column**)—the magnetic field amplitude. The amplitudes of the electric field at 10^5 V/m and magnetic field at 10^3 A/m are given in circles.

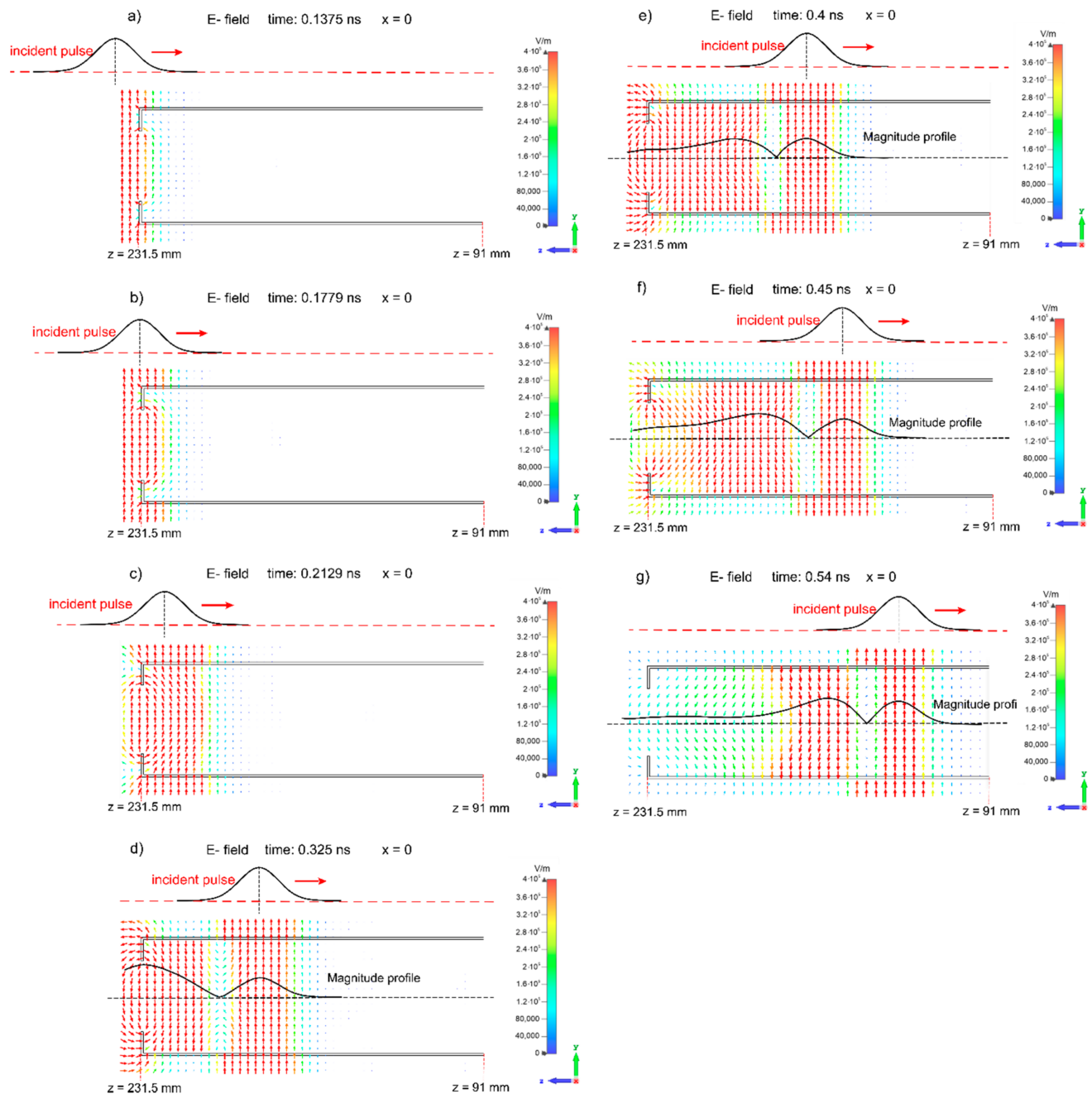


Figure 5. Vector maps of the electric field distribution in the plane $x = 0$ for various times (at $t = 0$ the incident plane wave pulse onset reached the front plane of the enclosure). (a) $t = 0.1375$ ns (the half-maximum of the front part of the incident pulse passed the enclosure front plane), (b) $t = 0.1779$ ns (the incident pulse maximum passed the enclosure front plane), (c) $t = 0.2129$ ns (the half-maximum of the rear part of the incident pulse passed the enclosure front plane), (d) $t = 0.325$ ns (the incident pulse fully passed the enclosure front plane), (e) $t = 0.4$ ns, (f) $t = 0.45$ ns, and (g) $t = 0.54$ ns—the incident pulse continued to move away from the enclosure front plane.

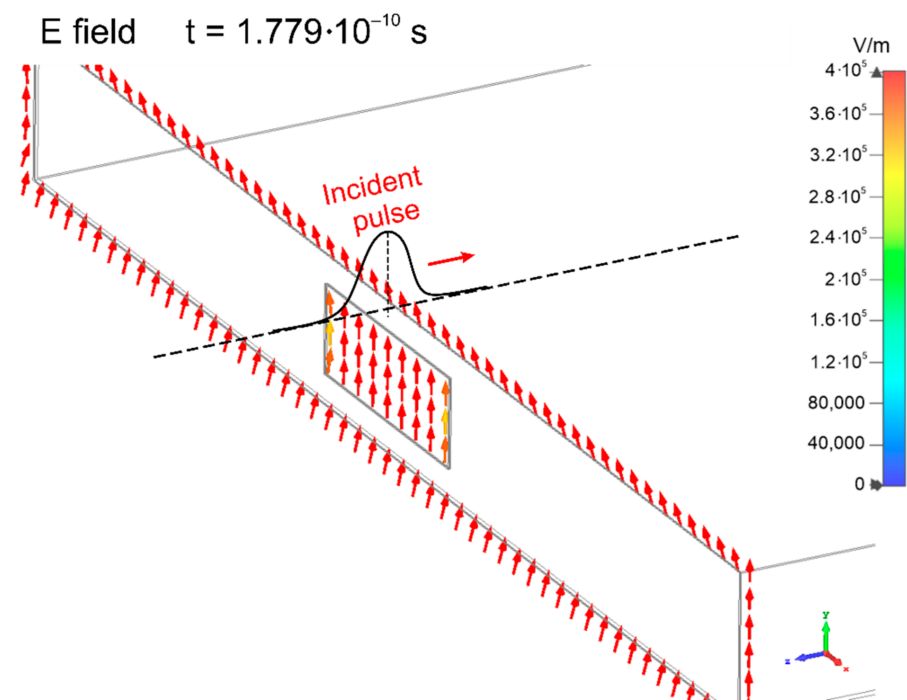


Figure 6. The electric field strength in the aperture of the shielding enclosure ($z = 231$ mm, $t = 0.1775$ ns). The electric field amplitude in the enclosure was equal to that of the incident pulse (10^6 V/m). The current position of the incident pulse is shown. Retrieved from Figure 3Eb.

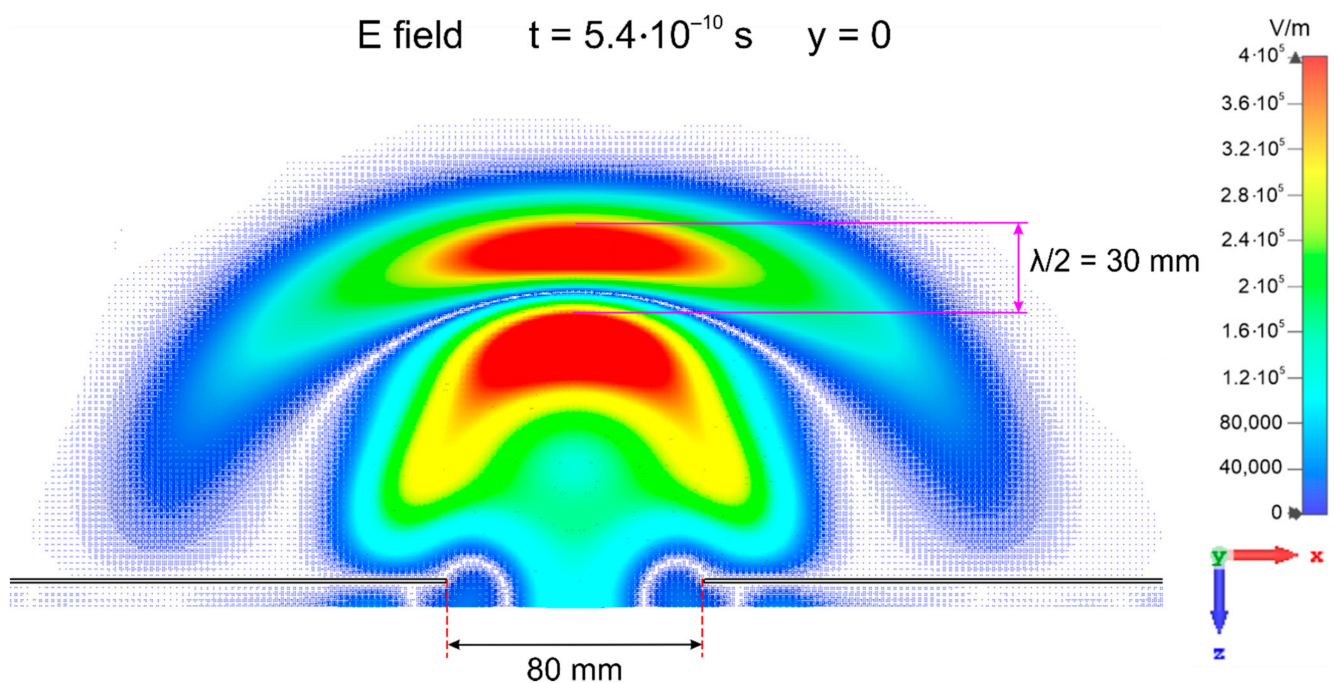


Figure 7. The electric field strength amplitude in the x-z plane for $y = 0$ at $t = 0.54$ ns near the front wall is shown.

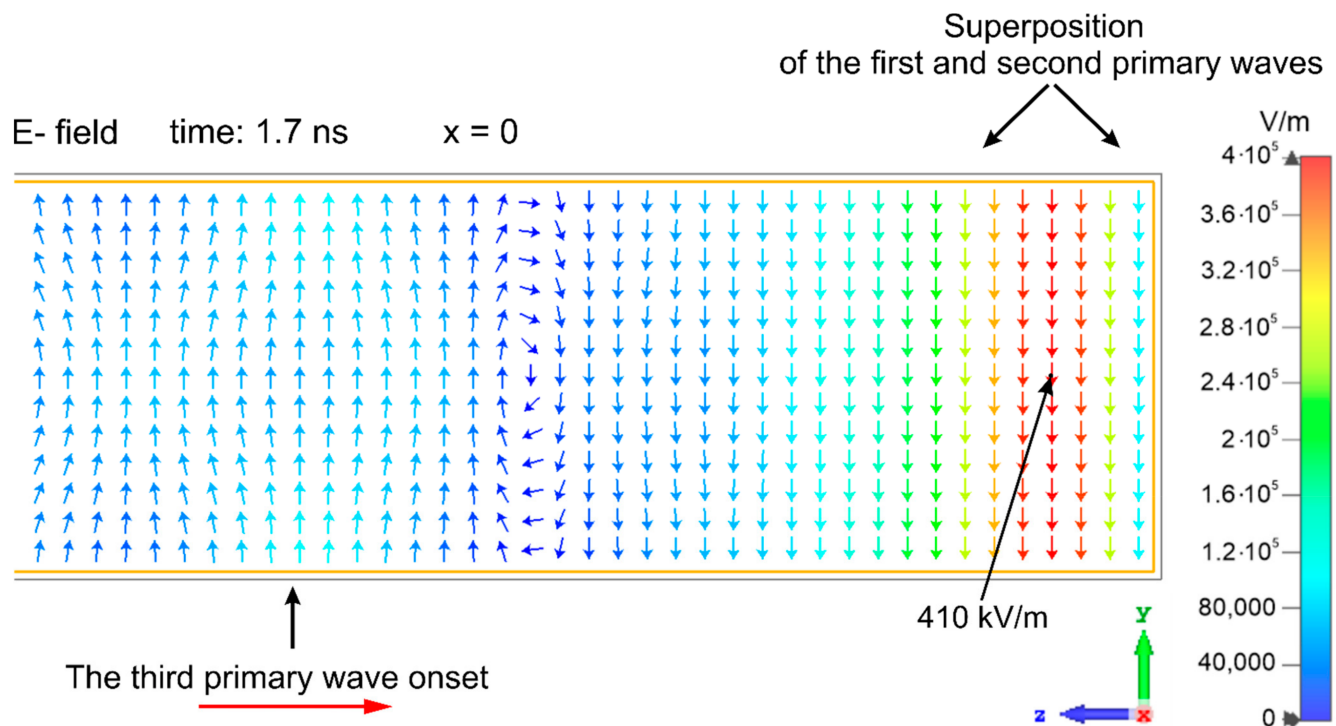


Figure 8. The electric field strength amplitude in the y - z plane for $x = 0$ at $t = 0.54$ ns, close to the rear wall, is shown. The figure shows the first interference of the waves P1 and P2 (for $t = 1.7$ ns). Retrieved from Figure 3Ek.

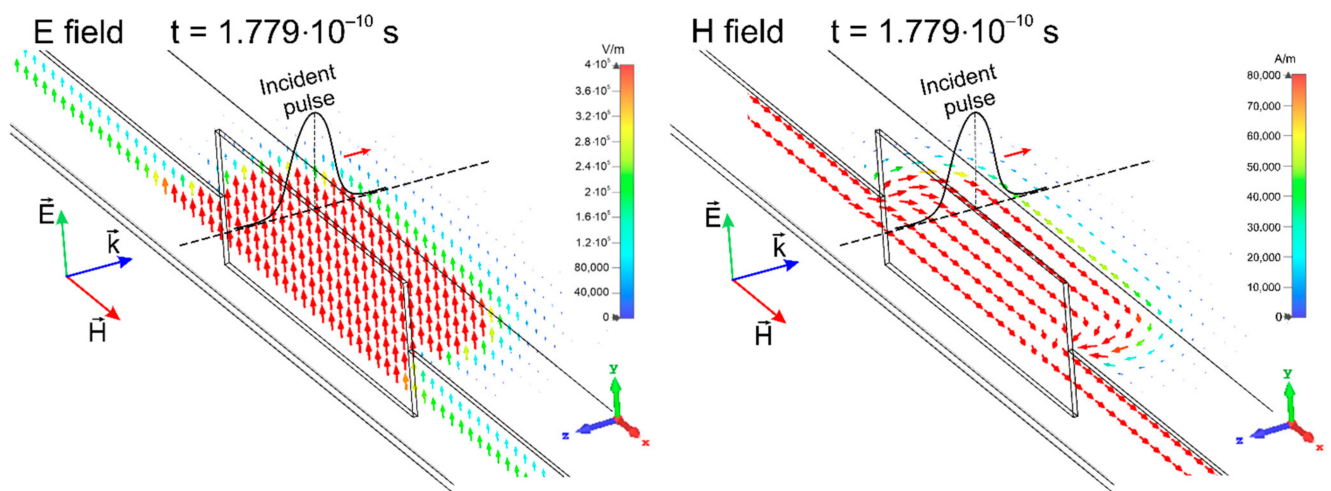


Figure 9. Associated electric \vec{E} and magnetic \vec{H} fields shown separately at $t = 0.1779$ ns (i.e., when the incident pulse maximum passed the enclosure front wall plane). The primary wave P1 was not yet fully developed (the phase just before the detachment from the aperture). Vector \vec{k} shows the propagation direction of the incident pulse. Retrieved from Figure 4Eb,Hb.

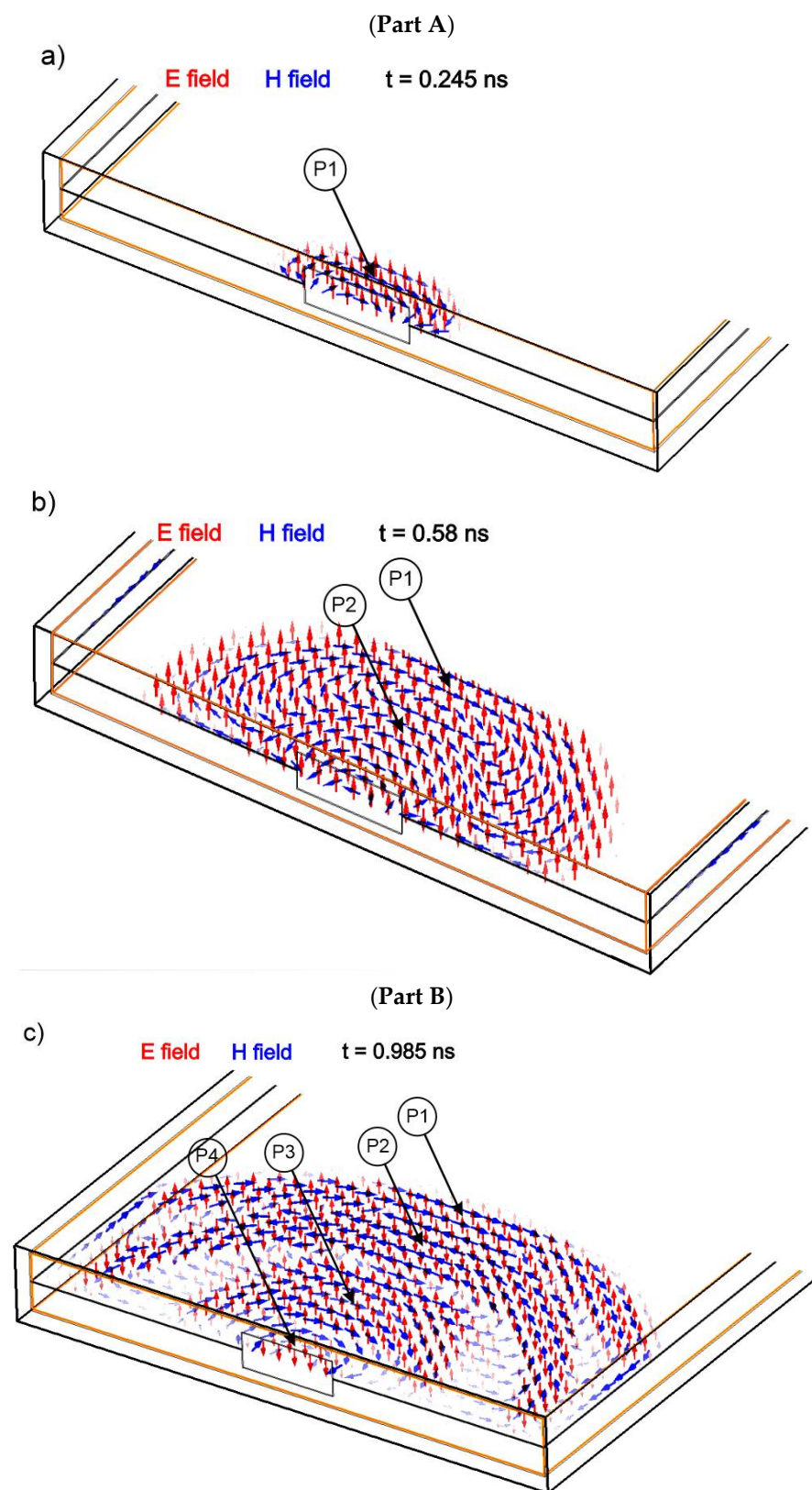


Figure 10. Cont.

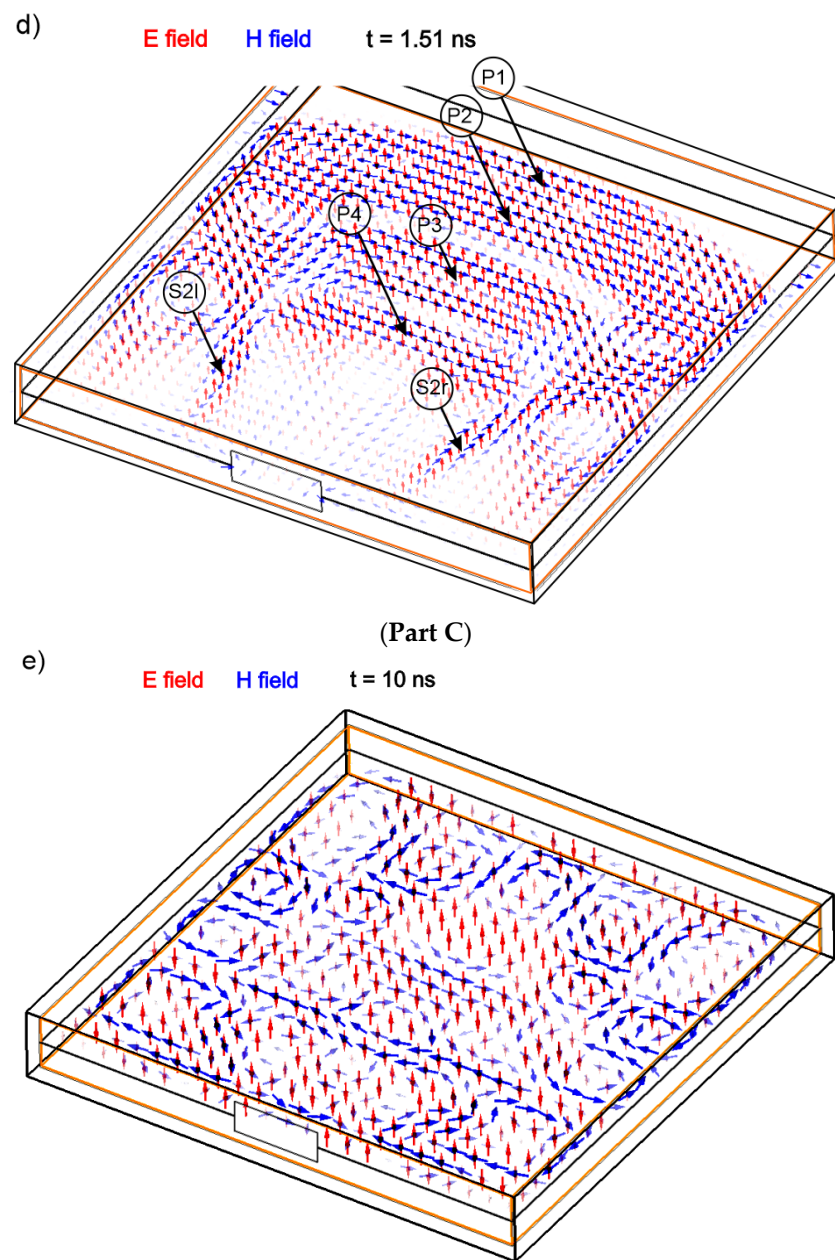


Figure 10. (Part A) Associated electric E and magnetic H fields for several selected cases showing: (a) the primary wave P1 detaching from the aperture ($t = 0.245 \text{ ns}$), (b) the primary waves P1 and P2 developed in the enclosure ($t = 0.58 \text{ ns}$). (Part B) Associated electric E and magnetic H fields for several selected cases showing: (c) the primary waves P1, P2, P3, and P4 present in the enclosure ($t = 0.985 \text{ ns}$), (d) the secondary waves S2l and S2r in the early interference stage ($t = 1.51 \text{ ns}$). (Part C) (e) Associated electric E and magnetic H fields showing the E and H field patterns in the developed interference stage ($t = 10 \text{ ns}$). Retrieved from Figure 4Es,Hs.

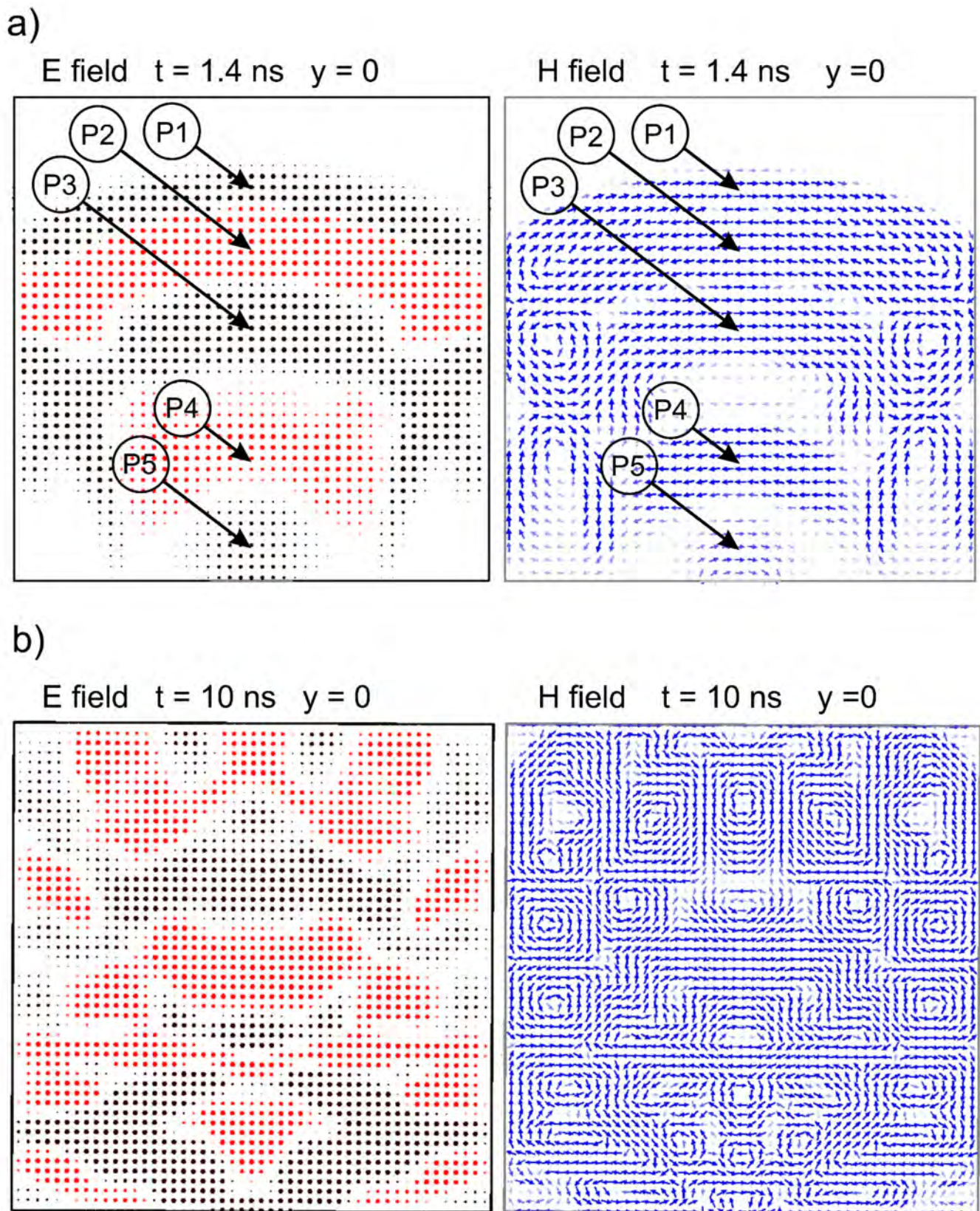


Figure 11. Electric and magnetic fields perpendicular to each other in the enclosure in the x - z plane ($y = 0$) at (a) $t = 1.4 \text{ ns}$ and (b) $t = 10 \text{ ns}$. Note the symmetrical arrangement of the field patterns with respect to the z -axis (i.e., to the line aperture center—the rear wall). The electric field vectors are perpendicular to the plane $y = 0$. The electric field vectors are marked by black points when directed into the figure and light red when directed in the opposite direction.

The electric field development inside the enclosure was limited in y direction by the presence of the lower and upper metallic walls. As a result, the electric field evolved into the y direction limited quasi-cylindrical waves that detached from the aperture (Figures 3Eb–Ed and 4Eb–Ed). At $t = 0.325$ ns, when the incident pulse fully passed the enclosure front wall plane and its direct effect on the enclosure aperture disappeared, there were two well-developed quasi-cylindrical waves inside the enclosure (Figures 3Ed, 4Ed and 5d). We call these the first (P1) and second primary waves (P2). In both waves, the electric field was directed in the y direction; the first wave P1 was polarized as the incident wave (i.e., in the $+y$ direction), while the second wave P2 was polarized in the opposite direction (in the $-y$ direction), as shown in Figure 5d. The distance between the wave fronts of both detached quasi-cylindrical waves can be considered as half the wavelength ($\lambda/2$). It is seen in Figure 7 (the cross section in the plane $y = 0$ at $t = 0.54$ ns) that the quasi-cylindrical wave half-length $\lambda/2 = 3$ cm. This corresponded to the height of the aperture, which behaved like a linear source of dipoles.

As time passed, in the time interval between $t = 0.56$ ns and $t = 0.96$ ns, two new, distinctly weaker waves were generated at the aperture (Figures 3Eg,Eh and 4Eg,Eh). We call these two waves the third (P3) and fourth (P4) primary waves. It cannot be ruled out that later even weaker primary waves may have appeared, but the spatial resolution and the associated image processing technique made it impossible to find their traces.

The electric field distribution in the primary wave was not uniform. The highest electric field amplitude was in the center of the wave. It decreased towards the wave front and back of the wave (Figure 5d–j) and in the direction of the wave wings (Figures 3Ed–Ej and 4Ed–Ej). The amplitude of the electric field of the second primary wave P2 at a given location in the enclosure was smaller than that of the first primary wave P1 passing through that location earlier.

All primary waves propagated towards the enclosure rear wall, simultaneously spreading laterally. Their volume increased, which caused the primary wave energy volume density to decrease. This was consistent with the decreasing values of the electric field strength of the waves (Figures 3Ed–Ej and 4Ed–Ej).

After around $t = 0.8$ ns, the left and right wings of the first primary wave P1 and then those of the second primary wave P2 reached the left and right sidewalls in the vicinity of the front corners of the enclosure (Figures 3Eg,Eh and 4Eg,Eh, at $t = 0.81$ ns and $t = 0.96$ ns, respectively). At this moment, the continuous reflection of the wings of the primary waves P1 and P2 from the sidewalls began. As a result, a part of the primary wave cut loose and formed a new wave at the left- and right-wing ends. We called these new waves secondary (S) waves. Figures 3Ei and 4Ei (at $t = 1.4$ ns) show two pairs of the reflected waves in their early development stage: the first was the left-side secondary S1l and the right-side secondary S1r waves, and the second was the left-side secondary S2l and the right-side secondary S2r waves. As seen from these figures, the secondary waves were directed diagonally towards the rear wall. After a short while (at $t = 1.5$ ns), when the wings of the primary wave P3 reached the sidewalls, a third pair of reflected waves S3l and S3r appeared (Figures 3Ej and 4Ej). The formation and development of the secondary waves can be traced more easily in the images showing the magnetic field development in the enclosure (Figures 3Hi,Hj and 4Hi,Hj).

After a partial loss of wings due to rebound on the sidewalls, the primary waves changed shape. Their wave fronts became flatter. The partial loss of wings also reduced the total energy of the primary waves (and correspondingly resulted in reduction of the electric field amplitude) (Figures 3Ei,Ej and 4Ei,Ej).

From the beginning of the first reflection of wings of the first primary wave P1 on the sidewalls and the formation of the first secondary waves S1l and S1r, caution should be exercised when interpreting images showing the structure of the electric (and magnetic) field in the enclosure. The images shown in Figures 3Ei and 4Ei and the following ones showed the interference patterns of the superimposed primary and secondary waves, thus hiding to some extent information about the primary and secondary waves, the behavior of

which thus far had been easy to observe. As will be shown, despite such an obstacle, tracing primary and secondary waves in the presence of the wave interference is not necessarily impossible in some cases. Generally, however, due to the wave interference, information about the wave nature of phenomena occurring in the enclosure will be lost to some extent.

At time $t = 1.54$ ns, the wave front of the first primary wave P1 reached the enclosure rear wall and then reflected back. The resulting electric field structure in the enclosure at $t = 1.7$ ns, i.e., just after the reflection of the first primary wave P1 at the rear wall is shown in Figures 3Ek and 4Ek. The maximum of the electric field amplitude ($4.1 \cdot 10^5$ V/m) in front of the enclosure rear wall at $t = 1.7$ ns (point B shown in Figure 1) was the result of the constructive superposition of the first primary wave P1 reflected from the rear wall and the second primary wave P2 traveling towards the rear wall. The map in Figure 8 is a vector representation of a moment of the constructive superposition of both waves at time $t = 1.7$ ns, which increased the electric field amplitude to $4.1 \cdot 10^5$ V/m in point B. It is worth noting that the maximum electric field amplitudes of the first P1 and second P2 primary waves during their travel towards the rear wall just before bouncing off from it were $2.68 \cdot 10^5$ V/m and $2.3 \cdot 10^5$ V/m, respectively (Figure 4Ei). The constructive superposition illustrated in Figure 8 was a consequence of the polarization change of the first primary wave P1 after bouncing off from the rear wall to opposite polarization, which was consistent with the polarization of the second primary wave P2 before its bouncing off from the rear wall.

Figures 3Ek and 4Ek (at $t = 1.7$ ns), Figures 3El and 4El (at $t = 1.8$ ns), and Figures 3Em and 4Em (at $t = 1.9$ ns) showed interference images of the electric field in the enclosure when the primary waves P1 and P2 travelled towards the front wall after their reflection from the rear wall and the secondary waves still moved towards the rear wall, i.e., in the opposite direction to the primary waves P1 and P2. Although the primary waves P1 and P2 experienced locally constructive and destructive interferences with the secondary waves in the period $t = 1.7$ – 1.9 ns, the fronts of the waves P1 and P2 can be identified against the background of various types of local interference patterns.

Figures 3Ek and 4Ek (at $t = 1.7$ ns), Figures 3El and 4El (at $t = 1.8$ ns), and Figures 3Em and 4Em (at $t = 1.9$ ns) showed that the secondary waves left the area of the enclosure in the vicinity of the front wall, moving towards the rear wall. Earlier, this area was left by the primary waves. At time $t = 2.55$ ns, the electric (and magnetic) field practically did not exist in almost half the volume of the enclosure facing the front wall (Figures 3En and 4En). Therefore, the primary waves P1 and P2, propagating towards the front wall, did not experience any interference in this area. This allowed for the location of the fronts of the waves P1 and P2 as they moved from almost the center of the enclosure until they reached the front wall (Figures 3Eo and 4Eo, $t = 3$ ns).

At time $t = 3.08$ ns, the primary wave P1 and, a little later, the primary wave P2 bounced off the front wall and returned towards the rear wall. Afterwards, reflections from the front wall experienced more waves traveling towards that wall, i.e., the remaining primary waves and the secondary waves. The former, after being reflected, turned back towards the rear wall, while the latter, after bouncing off the front wall towards the sidewalls, were reflected, and returned to the enclosure interior. At about $t = 4.35$ ns (Figures 3Ep and 4Ep), the primary wave P1 and the other waves following it towards the rear wall encountered an electric (and magnetic) field-free area in front of the rear wall, just like earlier on their way to the front wall (Figures 3En and 4En). The field-free area was left by the waves going towards the front wall. Since there was no interference in this area, the fronts of the primary waves P1 and P2 could be located in the vicinity of the rear wall (Figures 3Ep and 4Ep, $t = 4.35$ ns, and Figures 3Eq and 4Eq, $t = 4.7$ ns). Behind the primary waves P1 and P2, multiple constructive and destructive interferences of the other primary and secondary waves occurred inside the box, as illustrated by the interference patterns shown in Figures 3Ep,Eq and 4Ep,Eq.

Figures 3Er and 4Er show the electric field structure in the enclosure at time $t = 5$ ns, i.e., right after the second reflection of the first primary wave P1 from the rear wall. The

maximum of the electric field amplitude seen in front of the rear wall at time $t = 5$ ns was the result of the constructive superposition of the second primary wave P2 traveling towards the rear wall (after bouncing off the front wall) and the first primary wave P1 after its reflection from the rear wall.

The time $t = 5$ ns most likely terminated the time interval in which it is possible to locate the primary waves in the enclosure. After this time, the ever-increasing number of reflected waves produced such a large number of relatively strong interference patterns that it was impossible to find weakening primary waves. From this moment, we examine the development of the EM in the enclosure in terms of the associated electric and magnetic fields rather than magnetic and electric waves. Figures 3Es and 4Es (at $t = 10$ ns) to Figures 3Ex and 4Ex (at $t = 90$ ns) show that after $t = 5$ ns, the electric field distribution in the enclosure had an interference character, resulting from the constructive and destructive superposition of the steadily growing number of waves traveling across the enclosure after bouncing off the enclosure walls. The electric field distributions in the enclosure were temporally and spatially varying. They formed a symmetrical pattern in relation to the direction of the aperture—the rear wall (the z-axis), along which the primary waves and their residues traveled. Even after the primary waves substantially faded out, this symmetry seemed to hold due to the presence of a kind of wave-loss channel through the aperture. This could mean that the enclosure with aperture behaved like a kind of waveguide rather than an EM resonator.

The electric field E described above was accompanied by a magnetic field H (Figures 3Ha–Hx and 4Ha–Hx). In general, many of the above-presented features of the development of the electric field in the enclosure could be transferred to the description of the accompanying magnetic field development.

In the first phase (the wave phase) of the development of the EM field in the enclosure, the associated electric E and magnetic H fields formed primary and secondary EM waves (visible in Figures 3Ea–Eq, Ha–Hq and 4Ea–Eq, Ha–Hq). In the next development phase (the interference field), the EM field in the enclosure should rather be considered in terms of temporally and spatially varying patterns of the associated electric E and magnetic H fields (Figures 3Er–Ex, Hr–Hx and 4Er–Ex, Hr–Hx).

The association of the electric and magnetic fields can be easily seen in the wave phase of the EM development in the enclosure. It is understandable that, in the wave phase, each of the existing magnetic fields can be individually assigned to its associated electric field in a specific wave (Figures 9 and 10a–e). On the other hand, assigning a selected magnetic field to a specific electric field becomes more difficult or even impossible in the interference phase due to the large number of overlapping electric and magnetic fields (strengthening or weakening each other), which produces interference images that are difficult to interpret (e.g., in Figures 10e and 11b). In this case, the chosen magnetic field pattern can apparently be assigned to a number of patterns of the electric field.

In both development phases, the polarization planes of the electric and magnetic fields in the enclosure are compatible with the polarization planes of the electric and the magnetic fields of the incident wave pulse, respectively, i.e., the electric field is vertical and the magnetic field is horizontal with respect to the base (the largest wall) of the enclosure (Figures 9–11). The simulation results presented in Figures 9–11 show that, according to Maxwell's laws, the vectors of magnetic field H are perpendicular to the vectors of the electric field E and the magnetic field lines form closed loops (shown in Figure 11b, right).

Note that, in both development phases, an axial symmetry with respect to the z-axis (i.e., with respect to the direction from the aperture center towards the rear wall) of the arrangements of the electric and magnetic field patterns existed. This is clearly seen in Figures 9–11.

Similarly to the electric field, the magnetic field distributions in the enclosure were temporally and spatially varying. It can be noticed that both fields moved back and forth along the z-axis, not only in the wave phase, which is obvious, but also even when the primary and secondary waves substantially faded out. The careful observation of the

videos showing the dynamics of the development of the electric and magnetic fields in the enclosure revealed the axial movement of the electric and magnetic patterns, also in the deep stage of the interference phase (also recorded at $t = 90$ ns). As mentioned above, this was most likely caused by the presence of a wave-loss channel through the aperture.

The results presented in Figures 3Ea–Ex,Ha–Hx and 4Ea–Ex,Ha–Hx show that the amplitudes of the electric and magnetic fields in the enclosure with aperture were lower than those of the incident EM plane wave pulse (10^6 V/m and $2.68 \cdot 10^3$ A/m, respectively). They substantially decreased within 90 ns after the interference of the EM plane wave pulse to about $3.5 \cdot 10^4$ V/m and $1.5 \cdot 10^2$ A/m, respectively, at time $t = 90$ ns (Figure 4Ex,Hx). In the wave phase of the EM field development, the highest electric and magnetic fields in the enclosure occurred locally on the z-axis, decreasing from the aperture towards the rear wall (Figures 3Ea–Ej,Ha–Hj and 4Ea–Ej,Ha–Hj). In the interference phase, the electric and magnetic field distributions had the form of size-limited field patterns placed symmetrically with respect to the z-axis (Figures 3Ek–Ex,Hk–Hx and 4Ek–Ex,Hk–Hx). However, in this case, the highest electric and magnetic fields in the enclosure were also found on the z-axis; for example, at point B (0, 0, -211.5 ; Figure 1) (Figures 3Ek,Hk and 4Ek,Hk for $t = 1.7$ ns; Figures 3Er,Hr and 4Er,Hr for $t = 5$ ns).

6. Conclusions

This paper aimed at a better understanding of the coupling and development mechanisms of the EM field induced inside a small enclosure with aperture after the ultrashort interference caused by the subnanosecond transient high-energy EM plane wave pulse, which is vital for assessment of the shielding effectiveness of the enclosure with aperture under ultrashort transient interference conditions. Thus far, the case of the interaction of ultrashort transient high-energy EM pulse with the shielding enclosure with aperture has been poorly studied, in contrast to those of much longer pulses (longer than 150 ns). We define the ultrashort transient pulse as that for which duration is much shorter than the time that the pulse takes to pass the enclosure.

The numerical simulation of the coupling and development of the EM field inside the enclosure resulted in 2D and 3D images, which are the first to visualize the temporal and spatial build-up of electric and magnetic fields in the shielding enclosure with aperture within 90 ns after the ultrashort transient interference.

The presented 2D and 3D images, showing the EM field morphology in a relatively long period of time, proved to be crucial for understanding the EM field build-up process inside the shielding enclosure with aperture. They enabled us to discover two unknown phases of the EM field build-up in the enclosure with aperture. We called these two phases the wave phase and the interference phase. In the wave phase, the EM field is generated in the form of so-called primary and secondary wave pulses, traveling towards the rear wall of the enclosure. In the wave phase, the electromagnetic field is generated in the form of what we have called primary and secondary wave pulses, traveling towards the back wall of the enclosure. In the interference phase, the EM field has the form of temporally and spatially varying pulse-like interference (size-limited) patterns of the associated electric and magnetic fields.

The EM field induced in the enclosure is long-lasting compared to the interference pulse duration. The amplitudes of the electric and magnetic fields decreased about three-fold in 5 ns and 30-fold in 90 ns, thus exhibiting a severe EM hazard for much longer than the external interference duration. For a long period of time, the highest EM field amplitudes would change their locations in the enclosure, which makes it difficult to assess the shielding effectiveness on the basis of classical definitions [14] but satisfactory when the external interference is periodic. Frequency domain, which is generally used for analyzing the EM shielding effectiveness under periodic interference conditions, does not provide direct and immediate information on the shielding effectiveness in the transient interference case. Although there have been some attempts to introduce time domain parameters to evaluate the shielding effectiveness for transient interferences [15–19], this issue is far

from being solved. The fast temporally and spatially varying EM fields induced in the enclosure with aperture by the subnanosecond transient interference, visualized in detail over a relatively long period of time in this paper, is a useful data source of knowledge when working on the introduction of time-domain parameters to avoid ambiguity when evaluating the transient shielding effectiveness in the case of the ultrashort EM interference.

Supplementary Materials: The following are available online at <https://www.youtube.com/playlist?list=PLF9elidkw1ncZOMTjtkUphs2hqrcaqIN>. Videos: (A) 3D electric field magnitude, (B) 3D Magnetic field magnitude, (C) 2D electric field magnitude, and (D) 2D magnetic field magnitude.



Author Contributions: Conceptualization, M.B. and J.M.; methodology, M.B. and J.M.; investigation, M.B. and J.M.; writing—original draft preparation, M.B. and J.M.; writing—review and editing M.B. and J.M.; visualization, M.B. and J.M.; supervision, M.B. and J.M. All authors have read and agreed to the published version of the manuscript.

Funding: The project was financed within the program of the Ministry of Science and Higher Education called “Regionalna Inicjatywa Doskonałości” in the years 2019–2022; the project number was 006/RID/2018/19 and the sum of financing was PLN 11870000.

Institutional Review Board Statement: Not applicable.

Informed Consent Statement: Not applicable.

Conflicts of Interest: The authors declare no conflict of interest.

References

1. Sabath, F. System oriented view on high-power electromagnetic (HPEM) effects and intentional electromagnetic interference (IEMI). In Proceedings of the XXIX URSI General Assembly, Chicago, IL, USA, 7–16 August 2008. Available online: <https://www.ursi.org/proceedings/procGA08/papers/E02p5.pdf> (accessed on 26 June 2021).
2. Giri, D.V.; Tesche, F.M. Classification of Intentional Electromagnetic Environments (IEME). *IEEE Trans. Electromagn. Compat.* **2004**, *46*, 322–328. [CrossRef]
3. International Electrotechnical Commission. *International Standard: IEC 61000-2-13. Electromagnetic Compatibility (EMC)—Part 2-13: Environment—High-Power Electromagnetic (HPEM) Environments—Radiated and Conducted*, 1st ed.; IEC: Geneva, Switzerland, 2005.
4. Giri, D.V.; Tesche, F.M. An Overview of High-Power Electromagnetic (HPEM) Radiating and Conducting Systems. *Circuit Electromagn.* **2006**, *2006*, 1–19.
5. Kopp, C.; Pose, R. *The Impact of Electromagnetic Radiation Considerations on Computer System Architecture*; Department of Computer Science, Monash University: Clayton, VIC, Australia, 2016.
6. Sabath, F. *Threads of Electromagnetic Terrorism*; EUROEM 2012, Book of Abstracts; EUROEM 2012—ONERA: Toulouse, France, 2012.
7. Goldsman, N. *High Power Microwave Technology and Effects, Short Course Presented to MSIC Redstone Arsenal*; University of Maryland: College Park, MD, USA, 2005.
8. Hwang, S.M.; Hong, J.I.; Huh, C.S. Characterization of the susceptibility of integrated circuits with induction caused by high power microwaves. *Prog. Electromagn. Res. PIER* **2008**, *81*, 61–72. [CrossRef]
9. Fei, X.; Bing, C.; Chenglong, L. Damage efficiency research of PCB components under strong electromagnetic pulse. *Appl. Mech. Mater.* **2012**, *130–134*, 1383–1386.
10. Nitsch, D.; Sabath, F.; Schmidt, H.-U.; Braun, C. Comparison of the HPM and UWB Susceptibility of Modern Microprocessor Boards. *Syst. Des. Assess.* **2002**, *15*, 121–126.
11. Baum, C.E.; Nitsch, D.H. Band ratio and frequency domain norms. Air Force Office of Scientific Research, Wright-Patterson Air Force Base: Montgomery, OH, USA, 2003; Volume 584.
12. Cellozi, S.; Araneo, R. Alternative definitions for the time-domain shielding effectiveness of enclosures. *IEEE Trans. Electromagn. Compat.* **2014**, *56*, 483–485. [CrossRef]
13. Available online: www.cst.com (accessed on 26 June 2021).

14. IEEE Electromagnetic Compatibility Society (WG299—Working Group for Electromagnetic Shielding Enclosures, Working Group: Maria Sarto). *Standard Methods for Measuring the Effectiveness of Electromagnetic Shielding Enclosure*; IEEE Standard 299; IEEE Standard: Piscataway, NJ, USA, 2007.
15. Celozzi, S. New figures of merit for the characterization of the performance of shielding enclosures. *IEEE Trans. Electromagn. Compat.* **2004**, *46*, 142. [[CrossRef](#)]
16. Marvin, A.C.; Dawson, J.F.; Ward, S.; Dawson, L.; Clegg, J.; Weissenfeld, A. A proposed new definition and measurement of the shielding effect of equipment enclosures. *IEEE Trans. Electromagn. Compat.* **2004**, *46*, 459–468. [[CrossRef](#)]
17. Klinkenbusch, L. On the shielding effectiveness of enclosures. *IEEE Trans. Electromagn. Compat.* **2005**, *47*, 589–601. [[CrossRef](#)]
18. Araneo, R.; Celozzi, S. *Toward a Definition of Shielding Effectiveness in the Time Domain*; IEEE International Symposium on Electromagnetic Compatibility: Denver, CO, USA, 2013.
19. Celozzi, S.; Araneo, R. TD-Shielding effectiveness of enclosures in presence of ESD. In Proceedings of the International Symposium on Electromagnetic Compatibility, Brugge, Belgium, 2–6 September 2013; pp. 541–544.